



저작자표시-비영리-변경금지 2.0 대한민국

이용자는 아래의 조건을 따르는 경우에 한하여 자유롭게

- 이 저작물을 복제, 배포, 전송, 전시, 공연 및 방송할 수 있습니다.

다음과 같은 조건을 따라야 합니다:



저작자표시. 귀하는 원저작자를 표시하여야 합니다.



비영리. 귀하는 이 저작물을 영리 목적으로 이용할 수 없습니다.



변경금지. 귀하는 이 저작물을 개작, 변형 또는 가공할 수 없습니다.

- 귀하는, 이 저작물의 재이용이나 배포의 경우, 이 저작물에 적용된 이용허락조건을 명확하게 나타내어야 합니다.
- 저작권자로부터 별도의 허가를 받으면 이러한 조건들은 적용되지 않습니다.

저작권법에 따른 이용자의 권리는 위의 내용에 의하여 영향을 받지 않습니다.

이것은 [이용허락규약\(Legal Code\)](#)을 이해하기 쉽게 요약한 것입니다.

[Disclaimer](#)

이학박사 학위논문

**Subseasonal, interannual, and
long-term trend relationship
between Arctic and Eurasian
climate variability**

북극과 유라시아 기후 변동성 사이의 계절내, 경년
및 장기트렌드 관계

2021년 8월

서울대학교 대학원
지구환경과학부

김혜진

**Subseasonal, interannual, and
long-term trend relationship
between Arctic and Eurasian
climate variability**

**By
Hye-Jin Kim**

**A Dissertation submitted to the Faculty of the
Graduate School of the Seoul National University
in partial fulfillment of the requirements for the
Degree of Doctor of Philosophy**

**Degree Awarded:
April 2021**

Advisory committee:

**Professor Wookap Choi, Chair
Professor Seok-Woo Son, Advisor
Professor Kwang-Yul Kim
Professor Jong-Seong Kug
Professor Woosok Moon**

Subseasonal, interannual, and long-term trend relationship between Arctic and Eurasian climate variability

북극과 유라시아 기후 변동성 사이의 계절내, 경년 및 장기트렌드 관계

지도교수 손석우

이 논문을 이학박사 학위논문으로 제출함

2021년 4월

서울대학교 대학원
지구환경과학부
김혜진

김혜진의 이학박사 학위논문을 인준함

2021년 4월


위원장

부위원장

위원

위원

위원



Abstract

The statistical relationship between Arctic and Eurasian surface air temperature (SAT) has been observed in multiple time scale, from subseasonal to multi-decadal time scales. This relationship and the underlying mechanisms are revisited using reanalysis data and climate model experiments. Since the possible mechanisms could differ by the time scale, the subseasonal and interannual-to-long term trend relationship are investigated separately.

The subseasonal relationship between Arctic and Eurasian SAT is re-examined first. Consistent with previous studies, a significant negative correlation is observed in cold season from November to February, but with a local minimum in late December. This relationship is dominated not only by the warm Arctic-cold Eurasia (WACE) pattern, which becomes more frequent during the last two decades, but also by the cold Arctic-warm Eurasia (CAWE) pattern. The budget analyses reveal that both WACE and CAWE patterns are primarily driven by the temperature advection associated with sea level pressure anomaly over the Ural region, partly cancelled by the diabatic heating. It is further found that, although the anticyclonic anomaly of WACE pattern mostly represents the Ural blocking, about 20% of WACE cases are associated with nonblocking high pressure systems. This result indicates that the Ural blocking is not a necessary condition for the WACE pattern, highlighting the importance of transient weather systems in the subseasonal Arctic-Eurasian SAT co-variability.

The interannual-to-long term trend relationship between the Arctic and Eurasia is also investigated. Unlike the subseasonal Arctic-Eurasian relationship, Arctic sea ice is likely attribute to the recent Eurasian winter SAT change on interannual-to-decadal time scale. The present study quantifies the statistical relationship between Arctic sea-ice loss and Eurasian winter surface air-temperature change by a break-point trend analysis and maximum covariance analysis. A significant time-lagged covariability is observed between the Arctic sea-ice concentration over the Barents–Kara seas and the Eurasian winter surface air temperature, with the former leading the latter by approximately two months. More importantly, the timing of an abrupt decline in the autumn Arctic sea ice that occurred in the late 1990s is coincident with the beginning of the Eurasian winter cooling. This concurrent trend change is statistically significant and robustly found in both the break-point analysis and maximum covariance analysis. These results suggest that both the interannual variability and decadal trend change of the Eurasian winter surface air temperature are likely influenced by regional sea-ice changes over the Barents–Kara seas.

However, climate models often fail to reproduce the impact of Arctic sea ice change on Eurasian winter cooling in historical simulations. The present study re-examines the impact of Arctic sea ice loss on the Eurasian winter SAT trend by isolating the effect of the sea ice loss in coupled model simulations. In the large ensemble simulations, Eurasian winter cooling is observed in only half of the ensemble members, whereas others show warming trend, resulting in a near-zero trend when all 35 ensemble members are averaged. The cooling trend appears when the polar warming is not confined to the near-surface but extends

deep into the upper troposphere with a hint of stratospheric warming. When the polar warming is shallow in the model, the Eurasian SAT trend becomes positive. This result suggests that Eurasian winter cooling in the recent past is most likely caused by atmospheric internal variability, and highly dependent on the vertical extent of a polar warming and stratospheric processes, rather than Arctic surface warming itself.

Keywords : warm Arctic-cold Eurasia, Ural blocking, transient anomaly, Arctic sea ice loss, internal variability, deep Arctic warming

Student Number : 2016-37590

Table of Contents

| | |
|---|------------|
| Abstract..... | i |
| Table of Contents | iv |
| List of Tables..... | vi |
| List of Figures..... | vii |
| | |
| Overview..... | 1 |
| | |
| 1. Subseasonal relationship of Arctic and Eurasia..... | 3 |
| 1.1. Introduction | 3 |
| 1.2. Data..... | 6 |
| 1.3. Methodology | 7 |
| 1.3.1. Lead-lag regression | 7 |
| 1.3.2. Case selection..... | 8 |
| 1.3.3. Temperature tendency equation..... | 10 |
| 1.4. Results | 11 |
| 1.4.1. Subseasonal relationship of Arctic and Eurasian SAT | 11 |
| 1.4.2. Possible mechanisms of subseasonal relationship..... | 15 |
| 1.4.3. Seasonality of the subseasonal co-variability..... | 28 |
| 1.4.4. Subseasonal variability of the subseasonal co-variability..... | 30 |
| 1.4.5. Decadal variability of the subseasonal co-variability..... | 33 |

| | |
|--|-----------|
| 2. Interannual and long-term trend relationship of Arctic and Eurasia..... | 35 |
| 2.1. Introduction | 35 |
| 2.2. Data..... | 39 |
| 2.3. Methodology | 41 |
| 2.3.1. Break poing analysis | 41 |
| 2.3.2. MCA analysis..... | 43 |
| 2.3.3. Decomposition of a linear trend..... | 46 |
| 2.3.4. Blocking index..... | 47 |
| 2.4. Climate model simulations | 48 |
| 2.5. Results | 49 |
| 2.5.1. Interannual and long-term trend relationship of Arctic and Eurasian SAT | 49 |
| 2.5.2. Polar restoring experiments in GFDL CM2.1..... | 63 |
| 2.5.3. Long-term trend in polar restoring experiments..... | 67 |
| 2.5.4. Interannual variability in polar restoring experiments..... | 80 |
| 3. Summary and Discussion | 84 |
| References..... | 87 |
| 국문초록..... | 101 |
| 감사의 글 | 103 |

List of Tables

Table 1.1. The number of blocking related WACE cases and the ratio to the entire WACE cases.

Table 2.1. SCF, CC, percent variances of SIC and SAT, and their significant levels explained by the first leading mode derived from the maximum covariance analysis (MCA) for SON to DJF SICs and DJF SAT.

List of Figures

Figure 1.1. Correlation coefficients of (a) SAT and (b) SLP with respect to daily SAT anomalies averaged over the BKS for the period from 1979/1980 to 2016/2017 NDJF. Only the values that are statistically significant at the 95% confidence level are shaded. The analysis domains of the BKS and the Eurasian continent are denoted with boxes in (a). Likewise, the Ural region is denoted with a box in (b).

Figure 1.2. Lead-lag regression coefficients of BKS and Eurasian SAT anomalies during the period of 1980-2016. The y-axis is the starting day of the 30-day combined time series and the x-axis is the time lag. Only the values that are statistically significant at the 95% confidence level are shaded.

Figure 1.3. Lead-lag regression coefficients of (a) Eurasian SAT and (b) Ural SLP anomalies onto BKS SAT anomalies during the period of 1980-2016. The y-axis is the starting day of the 30-day combined time series and the x-axis is the time lag. Only the values that are statistically significant at the 95% confidence level are shaded.

Figure 1.4. The lead-lag composite mean of SAT (shaded) and SLP (contour) anomalies and wind (vector) anomalies at 850 hPa for (left) WACE and (right) CAWE cases at lags (a-b) -6 days, (c-d) -4 days, (e-f) -2 days, (g-h) 0 days, (i-j) 2 days, and (k-l) 4 days with respect to the local maximum of DI. The contour interval for SLP anomalies is 2 hPa and the negative values are contoured in dashed line. Only the values that are statistically significant at the 95% confidence level are shaded.

Figure 1.5. Same as Figure 1.4. but for (left) WACE with blocking and (right) without blocking cases.

Figure 1.6. (a-b) The SAT tendency, (c-d) T850 tendency, (e-f) horizontal temperature advection, (g-h) diabatic heating, (i-j) adiabatic heating averaged

from -5 to 0 days for (left) WACE and (right) CAWE cases. Note that all values are slightly smoothed by applying a nine-point local smoothing once and the underground values are excluded. Only the values that are statistically significant at the 95% confidence level are shaded.

Figure 1.7. (a) Time evolution of lead-lag composites of BK (black) and Eurasian (gray) SAT (solid line) and T850 (dashed line) and Ural SLP (blue) for the WACE cases. Lead-lag composites of temperature tendency and budget terms in (c) BK seas and (e) Eurasia. (b,d,f) Same as in (a,c,e) but for CAWE cases. The statistically significant values at the 95% confidence level are bolded.

Figure 1.8. Same as Figure 1.7 but for WACE cases with and without blocking.

Figure 1.9. The time-integrated temperature tendency and budget terms for lag -5 to 0 days over (a-b) BKS and (c-d) Eurasia for (left) WACE and (right) CAWE cases.

Figure 1.10. The composite mean of SAT anomalies (shaded) and T850 climatology (contour) for the high Ural SLP cases in (a) NDJF and (b) JJA. The contour interval for T850 climatology is 6K.

Figure 1.11. Regression coefficient (blue) at +2 days in Figure 1.2. and the standard deviation of Ural SLP anomalies. The y-axis is the starting day of the 30-day combined time series. Only the values that are statistically significant at the 95% confidence level are bolded in blue line.

Figure 1.12. Histogram of polar cap (north of 65°N) averaged geopotential height anomaly at 50 hPa for (a) WACE and (b) CAWE cases in January and February. For each WACE or CAWE case, lag -3 to 3 days are considered to obtain the histogram.

Figure 1.13. Frequency of the WACE (red) and CAWE (blue) cases during 1980 to 2017. Note that the last decade indicates the frequency of WACE and CAWE for 8 years of 2010-2017.

Figure 2.1. Area-mean SAT and its linear trend in DJF (blue) and JJA (red): (a) the Northern Hemisphere extratropics, (b) Eurasia and (c) North America. Dashed lines represent an extended trend in the absence of a breakpoint, and the black solid lines running parallel to the x-axis are the 95% confidence interval of the estimated break point indicated by the black dashed lines. The right column shows the DJF SAT trend (d) before and (e) after 1998. The values that are statistically significant at the 95% confidence level are dotted. Two boxes denote the Eurasian and North American domains.

Figure 2.2. (a) SON, (b) OND, (c) NDJ, and (d) DJF SIC and their linear trends over the BKS. The overall format is identical to that of Fig. 2.1a. Right panels show the linear trend in SIC in each season since 1998. The values that are statistically significant at the 95% confidence level are dotted. The boxes in the right column denote the domain of BKS.

Figure 2.3. (left) EC time series of the leading mode of the MCA and their trends of the (a) OND SIC and (b) DJF SAT. The overall format is identical to that of Fig. 2.1a. The numbers in the top right corners of (a) and (b) denote the correlation coefficients with the Barents-Kara SIC time series (Fig. 2.2b) or the Eurasian SAT time series (Fig. 2.1b). The right column shows the (c) homogeneous (OND SIC projection onto the leading EC time series of OND SIC) and (d) heterogeneous (DJF SAT projection onto the leading EC time series of OND SIC) maps for 1979-2013. Note that the latitudinal domain of (c) is different from that of (d).

Figure 2.4. Same as Figure 2.3(d) but for DJF (a) SLP, (b) Z500, and (c) Z50.

Figure 2.5. Lead-lag regression map of PCI Z onto the leading EC time series of OND SIC for 1979-2013.

Figure 2.6. (a) Linear trend in the DJF SAT, (b) the trend that is linearly congruent with the OND SIC trend over the BKS seas, and (c) the residual

component for 1998-2013. The values that are statistically significant at the 95% confidence level are dotted.

Figure 2.7. Seasonal cycle of Arctic (a) SST and (b) SIC in ERA-5 (green) and ensemble mean (black) and individual ensembles (gray) in CM2.1 polar restoring experiment. (c-d) same as in (a-b) but for BKS.

Figure 2.8. (a-b) Annual mean Arctic (70-90N) (a) SST and (b) SIC anomalies in ERA-5 (green) and ensemble mean (black) and individual ensembles (gray) in CM2.1 polar restoring experiment. (c-d) same as in (a-b) but for DJF season. (e-f) same as in (c-d) but for BKS.

Figure 2.9. DJF-mean (a) SAT, (b) SLP, (c) U300, and (d) blocking frequency trend over the 1986-2015 from ERA5. Only the values that are statistically significant at the 95% confidence level are dotted.

Figure 2.10. Same as Figure 2.9. but for the ensemble mean of 35 experiments in GFDL CM2.1.

Figure 2.11. Relationship of the Ural SLP trend to Eurasian SAT trend in ERA5 (green) and the ensemble mean (black) and individual ensemble members (grey) in GFDL CM2.1 for the period of 1986-2015. Note that the ensemble members of Ural+ group are denoted in light pink, while that in Ural- group are denoted in light blue. The ensemble means of Ural+ and Ural- are denoted in red and blue, respectively.

Figure 2.12. Same as Figure 2.11. but for BKS SAT trend.

Figure 2.13. Same as Figure 2.10. but for ensemble means of (left) Ural+ group and (right) Ural- group.

Figure 2.14. Vertical cross section of the zonally averaged DJF temperature trend over 1986-2015 in ensemble means of (a) Ural+ group and (b) Ural- group.

Only the values that are statistically significant at the 95% confidence level are dotted.

Figure 2.15. Same as Figure 2.11. but for the PCI_T averaged from 700 to 300 hPa.

Figure 2.16. Lead-lag correlation between the BKS SIC and Eurasian SAT for the period of 1986-2015 in observation (green), the ensemble mean (black), Ural+ mean (blue), and Ural- mean (red). The ensemble spreads are denoted in grey bars.

Figure 2.17. Correlation coefficient between the Ural SLP anomaly and PCI T anomaly averaged over the 700hPa to 300hPa for the period of 1986-2015 in observation (green), the ensemble mean (black), Ural+ mean (blue), Ural- mean (red), and individual ensembles (light colors). The Ural+ and Ural- ensemble members are denoted in light pink and light blue.

Overview

Arctic amplification, which is Arctic temperature raises more rapidly than lower latitude, has been intensified in recent decades (Cohen et al. 2014). The Arctic warming can possibly cause climate change over the high latitude. For instance, the drastic decreases in Arctic sea ice extent and thickness have been observed as a consequence of the Arctic warming (Stroeve et al. 2012). This Arctic sea ice change can amplify Arctic warming as surface albedo decreases over the Arctic, which causes more radiative energy absorbed in the atmosphere. This so-called ice-albedo feedback is one of the dominant factor contributing the Arctic warming in cold season.

However, the impacts of Arctic warming are not limited to the Arctic region. Previous studies suggested that the recent Arctic warming can affect midlatitude weather and climate. Francis and Vavrus (2012) argued that the Arctic amplification have reduced the meridional temperature gradient and this weakened temperature gradient causes the weak and meandering jet stream, which could result in the extreme cold winters. Based on the statistical relationship between the Arctic warming and midlatitude cooling, the Arctic warming has been suspected as a driver of the weather and climate change in midlatitude.

What is important here is that this statistical relationship between Arctic and Eurasia is observed in multiple time scales, from subseasonal to long-term time scale. In general, similar atmospheric phenomena with the different

temporal and spatial scales can be modulated by difference dynamical mechanisms. For instance, the cold weather in Eurasia is highly associated with the blocking high over the Ural region, while the Eurasian winter climate is linked with the Siberian high. Thus, to understand the impact of Arctic warming on the midlatitude weather and climate, this covariability is required to be discussed on individual time scales. This study aims to quantify the statistical association between Arctic and Eurasian surface air temperature and to understand the impact of Arctic warming on Eurasian weather and climate in subseasonal and interannual-to-long term time scale.

1. Subseasonal relationship of Arctic and Eurasia

1.1. Introduction

The warm Arctic-Cold Eurasia (WACE) pattern is well recognized as a dominant interannual climate variability in the boreal winter (Zhang et al. 2008; Mori et al. 2014; Kim and Son 2016). This seesaw-like surface air temperature (SAT) variability has recently received a significant attention due to the time lag. It was particularly found that the Arctic sea ice reduction and the resulting warm SAT anomaly over the Barents-Kara seas (BKS) often precede cold SAT anomaly over the Eurasia by a few months (Cohen et al. 2014; Kim et al. 2014; Overland et al. 2015; Kim and Son 2020). Such a relationship implies that Arctic climate variability can be used as a potential source for seasonal prediction of Eurasian SAT anomaly (Jung et al. 2014; Furtado et al. 2016), especially when combined with North Atlantic sea surface temperature (Matsumura and Kosaka 2019).

The WACE relationship also appears on the subseasonal time scale (Zhang et al. 2012; Wu et al. 2013; Kug et al. 2015; Luo et al. 2016a; Sorokina et al. 2016; Gong and Luo 2017; Yao et al. 2017; Luo et al. 2019; Tyrlis et al. 2020). Kug et al. (2015) showed that the low-frequency variability of BKS SAT typically leads Eurasian SAT by approximately two weeks. This time lag becomes much shorter if the high-frequency variability is considered. Luo et al. (2019), for instance, showed that daily BKS SAT anomaly accompanies Eurasian SAT anomaly with only one-day time lag. This short-term co-variability is not directly induced by Arctic sea ice loss but caused by atmospheric circulation (Luo et al. 2016a; Yao

et al. 2017; Tyrlis et al. 2020). A series of studies have shown that daily BKS sea ice change is a response to atmospheric circulation over the Ural region rather than a trigger (Sorokina et al. 2016; Gong et al. 2017; Tyrlis et al. 2020).

As a key driver of the subseasonal WACE pattern, the Ural blocking has been highlighted in the literature (Luo et al. 2016a; Luo et al. 2016b; Yao et al. 2017; Tyrlis et al. 2020). A blocking high can effectively generate an anti-correlation between BKS and Eurasian SAT anomalies by modulating the moisture and temperature advection, especially when the background wind or the potential vorticity gradient is weak (Luo et al. 2019; Yao et al. 2019). Physically, the Arctic warm anomaly has been often attributed to the increased downward longwave radiation by the enhanced moisture transport into the Arctic (Park et al. 2015; Yao et al. 2017; Chen et al. 2018). Likewise, Eurasian cold anomaly has been related to the reduced downward longwave radiation (Yao et al. 2017). However, warm anomaly in the Arctic, resulting from the Ural blocking could immediately increase the upward longwave radiation, resulting in a weak net longwave radiation (Kim et al. 2019). In this regard, other studies have suggested the temperature advection as a key driver (Panagiotopoulos et al. 2005; Mori et al. 2014; Ye and Messori 2020). The relative importance of the temperature advection and diabatic heating, however, is not well quantified.

Although the subseasonal WACE pattern has been related to the Ural blocking (Luo et al. 2016a; Luo et al. 2016b; Yao et al. 2017; Tyrlis et al. 2020), it is not clear whether the Ural blocking, which is quasi-stationary or slowly moves westward in time, is a necessary condition. A transient system that

travels eastward in time could also generate the WACE pattern. Such possibility, however, has not been addressed in the literature.

In this study, we revisit the daily relationship between Arctic and Eurasian SAT anomalies. Since the relationship could vary from month to month as background flow changes, its subseasonality is first examined. Unlike previous studies which have focused on the WACE pattern, both the WACE pattern and its opposite, the so-called cold Arctic-warm Eurasia (CAWE) pattern CAWE, are considered. Although the CAWE pattern is inferred from the mode of interannual SAT variability (Zhang et al. 2008; Mori et al. 2014; Kim and Son 2016), its spatio-temporal distribution and the driving mechanism have been rarely addressed on the subseasonal time scale.

When examining the WACE pattern, the presence of the Ural blocking is not presumed. Instead the WACE pattern associated with the Ural blocking is compared to that without blocking. The physical processes responsible for the WACE and CAWE patterns are then quantified by computing the temperature budget. The budget analysis reveals the relative importance of the temperature advection against the diabatic heating.

1.2. Data

The six-hourly and daily atmospheric variables, which include SAT, sea level pressure (SLP), geopotential height (Z), and zonal wind (U), are obtained from the European Centre for Medium-Range Weather Forecasts (ECMWF) Re-Analysis-Interim (ERA-Interim; Dee et al. 2011) for the period of 1979-2017. The spatial resolution of these data is $1.5^\circ \times 1.5^\circ$. The daily anomaly is defined as the deviation from the long-term climatology for each calendar day. The long-term trend is not removed here as its impact is minimal. Although not shown, overall results do not change much when the detrended data are utilized.

1.3. Methodology

1.3.1. Lead-lag regression

To investigate the optimal time lag between the two variables, a time-lagged linear regression analysis is applied:

$$y(d, t + \tau) = r(d, \tau)x(d, t) + \varepsilon(d, \tau) \quad (1)$$

where $r(d, \tau)$ is a regression coefficient of $y(d, t + \tau)$ with respect to $x(d, t)$ for the selected calendar day d ($= 1$ to 365 days) with time lag τ ($= -20$ to 20 days). The last term, $\varepsilon(d, \tau)$, is the residual. In Eq. (1), t is a regression window which is set to 30 days, starting from calendar day d . Here the calendar day d starts from 1 July 1979 to 30 June 1980 to examine the seasonal variability centered on winter. To keep the same length, the time series is constructed for 38 years starting from the selected d . For instance, if d is 1 July, the time series is constructed by combining the following 30 days (i.e., 1–30 July) from 1979 to 2016 ($30 \text{ days} \times 38 \text{ years} = \text{total of } 1,140 \text{ days}$). The statistical significance of the regression coefficient is evaluated with the Student's t-test. The effective number of degrees of freedom is determined by considering the autocorrelation (Bretherton et al. 1999).

1.3.2. Case selection

The composite analyses are further conducted for WACE and CAWE cases. These cases are first identified by computing the dipole index (DI):

$$DI = SAT_{BK} - SAT_{Eurasia} \quad (2)$$

where SAT_{BK} and $SAT_{Eurasia}$ are area-averaged SAT anomalies over BKS and Eurasia, respectively. The BKS domain is set to 30°–70°E and 70°–80°N, whereas the Eurasian domain is set to 50°–130°E and 35°–50°N from a daily correlation map (Fig. 1.1.). This definition is similar to the seasonal-mean WACE index used in some previous studies (Luo et al. 2016b; Outten and Esau 2012). When the WACE pattern is pronounced, DI is expected to be positive. The opposite is true for the CAWE pattern. Both WACE and CAWE cases are defined as a time period when the DI index exceeds one standard deviation for at least three consecutive days. The minimum interval between the DI maxima is set to 15 days to avoid duplicated selections. If multiple DI maxima are detected within 15 days, the largest one is selected as a case. The date of maximum (or minimum) DI index is assigned as the WACE (or CAWE) date, and the time lags from -10 to 10 days are allowed for the case composite. A total of 78 WACE cases (about 2.05 times per year) and 70 CAWE cases (about 1.84 times per year) are identified from November to February (NDJF).

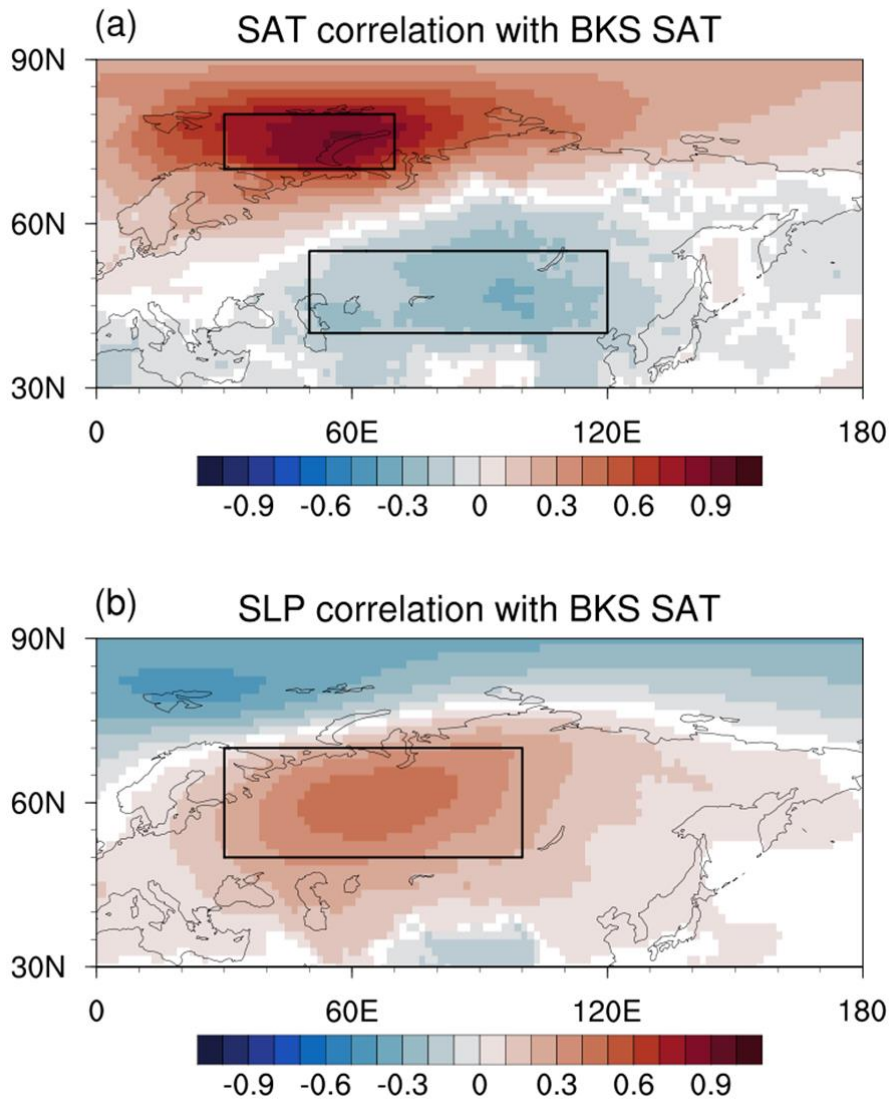


Figure 1.1. Correlation coefficients of (a) SAT and (b) SLP with respect to daily SAT anomalies averaged over the BKS for the period from 1979/1980 to 2016/2017 NDJF. Only the values that are statistically significant at the 95% confidence level are shaded. The analysis domains of the BKS and the Eurasian continent are denoted with boxes in (a). Likewise, the Ural region is denoted with a box in (b).

1.3.3. Temperature tendency equation

The Arctic-Eurasian SAT (co-)variability is investigated by computing the temperature tendency equation at 850 hPa:

$$\frac{\partial T}{\partial t} = -V_H \cdot \nabla_H T + S_p \omega + Q + \text{Res} \quad (3)$$

where $\partial T / \partial t$ is the temperature tendency at 850 hPa, horizontal advection $-V_H \cdot \nabla_H T$, adiabatic heating and vertical advection $S_p \omega$, diabatic heating Q , and residual Res . In Eq. (3), V_H is the horizontal wind vector, ω is the p-velocity, and S_p is the stability parameter represented by $S_p = (R/C_p)(T/p) - (\partial T / \partial p)$ where R is the gas constant for dry air ($=287 \text{ J kg}^{-1} \text{ K}^{-1}$) and C_p is the specific heat at constant pressure. Unlike other variables, Q is derived from the ECMWF forecast. The last term in Eq. (3), Res , includes both the forecast errors and the numerical errors. To clarify the mechanism for the temperature change over complex terrain, the same budget analysis is applied at 925hPa. Each budget term is calculated using six-hourly raw data and averaged into daily. The daily anomalous budget is examined, instead of the raw daily budget, in order to quantify the contribution of individual terms to the temporal evolution of temperature tendency.

1.4. Results

1.4.1. Subseasonal relationship of Arctic and Eurasian SAT

Figure 1.2 shows the time-lagged regression coefficients between the BKS and Eurasian SAT anomalies as a function of the calendar day (see section 2.2.1). A significant negative relationship appears in the cold season (Fig. 1.2). Such relationships, which are evident only from November to February, are maintained for over a month, indicating that their time scale is longer than a synoptic scale. This result also suggests that WACE/CAWE relationships is unique only in the boreal winter. Although not shown, the same analyses with other reanalysis data show essentially the same results.

The BKS-Eurasian SAT anomalies exhibit a maximum co-variability at lag +2 days, the former leading the latter (Fig. 1.2). The similar lags ranging from +1 to +5 days, depending on the analysis domain, are also found in previous studies (Yao et al. 2017; Luo et al. 2019). This lagged relationship, however, does not indicate that the Arctic sea ice or sea surface temperature condition drives the Eurasian SAT variability. Although the BKS SAT anomalies are closely related to local sea ice and sea surface temperature anomalies, they often lead the Arctic surface condition on a daily time scale (Luo et al. 2019; Tyrlis et al. 2020).

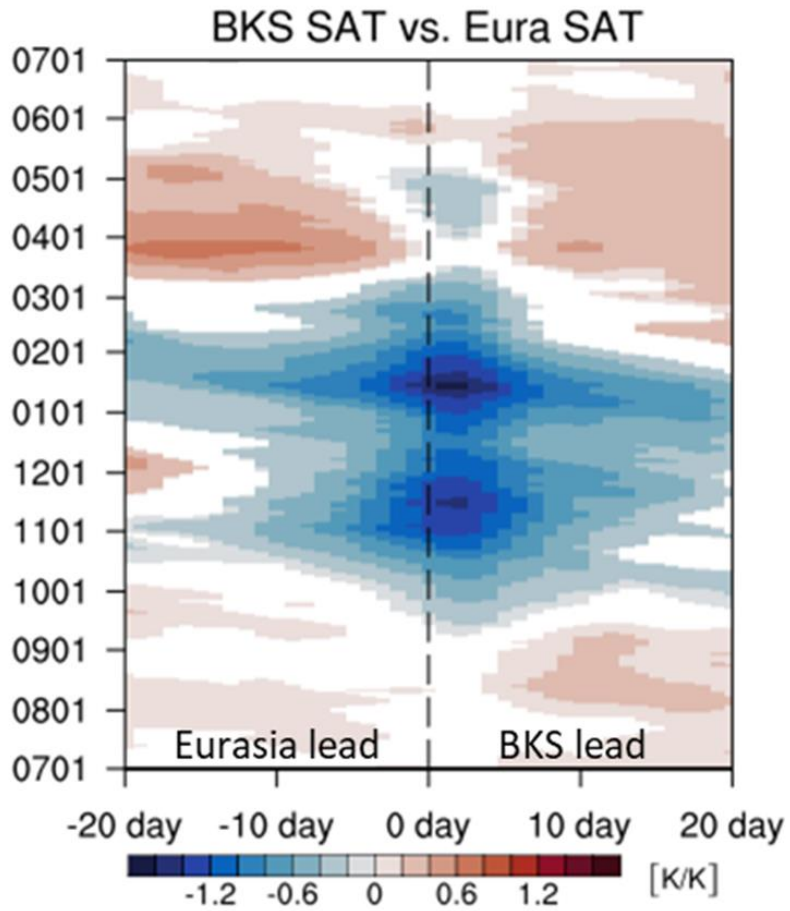


Figure 1.2. Lead-lag regression coefficients of BKS and Eurasian SAT anomalies during the period of 1980-2016. The y-axis is the starting day of the 30-day combined time series and the x-axis is the time lag. Only the values that are statistically significant at the 95% confidence level are shaded.

The lagged relationship is instead largely driven by the SLP anomaly over the Ural region (Gong and Luo 2017; Luo et al. 2019; Tyrlis et al. 2020). Figures 1.3a and b show strong positive correlations between the BKS SAT and Ural SLP anomalies and negative correlations between the Eurasian SAT and Ural SLP anomalies, respectively. Here the Ural SLP anomaly is calculated over 30°-100°E and 50°-70°N (Fig. 1.1). While no time lag is observed in Fig. 1.3a, a 2-day time lag is evident in Fig. 1.3b. This result suggests that the lagged relationship of the BKS-Eurasian SAT anomalies is caused by the delayed response of the Eurasian SAT to the Ural SLP anomalies. This result is consistent with previous studies (Zhang et al. 2012; Yao et al. 2017; Luo et al. 2019; Tyrlis et al. 2020), showing that the WACE-like SAT pattern is mainly caused by the blocking high over the Ural region rather than the short-term sea ice variability. However, our analysis does not presume the presence of blocking, generalizing the previous findings which are based on blocking composites.

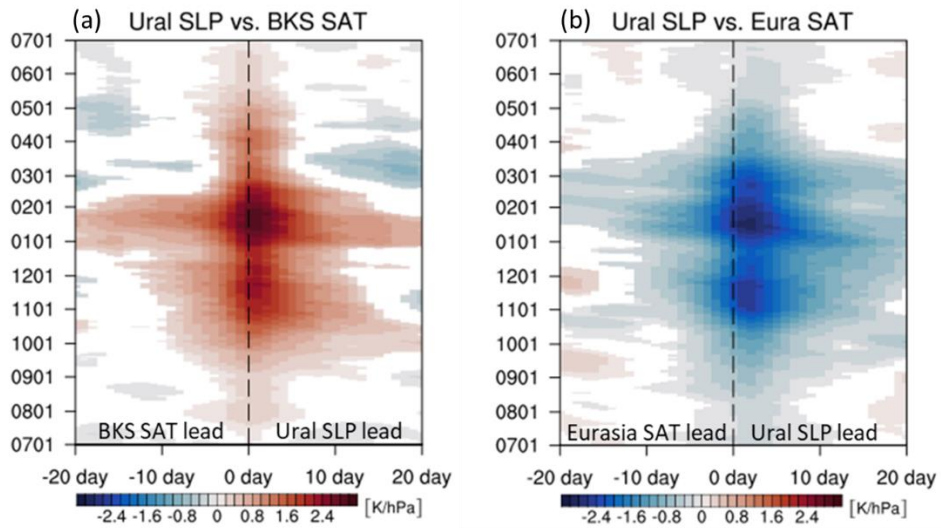


Figure 1.3. Lead-lag regression coefficients of (a) Eurasian SAT and (b) Ural SLP anomalies onto BKS SAT anomalies during the period of 1980-2016. The y-axis is the starting day of the 30-day combined time series and the x-axis is the time lag. Only the values that are statistically significant at the 95% confidence level are shaded.

1.4.2. Possible mechanisms of subseasonal relationship

The co-variability of the BKS-Eurasian SAT anomalies is further illustrated in Fig. 1.4 for WACE and CAWE cases separately. Here, only the boreal winter, NDJF, is considered for the case selection. A strong warm anomaly over the BKS and a cold anomaly over the Eurasia are well defined in the WACE cases. Unlike the BKS SAT anomaly, the Eurasian SAT anomaly expands southeastward in time. This temporal evolution is in agreement with the time lag between the Ural SLP and Eurasian SAT anomalies shown in Fig. 1.3b.

The anticyclonic anomaly over the Ural region is quasi-stationary and maintained over 10 days, representing the Ural blocking (Luo et al. 2016b; Yao et al. 2017). To quantify the contribution of the Ural blocking to the WACE SAT variability, the WACE cases are grouped into those with and without the Ural blocking. Here, the blocking is identified with the Tibaldi-Molteni index (Tibaldi and Molteni 1990), which is defined as a gradient reversal of geopotential height at 500 hPa from south ($\phi_S=40^\circ\text{N} + \Delta$) to north ($\phi_N=80^\circ\text{N} + \Delta$). The choice of Δ is from -4.5° to 4.5° in 1.5° increment. The Ural blocking is identified when the gradient reversal persists more than three consecutive days over the longitude band of $30\text{-}100^\circ\text{E}$. The blocking-related WACE cases are then classified when the Ural blocking is detected within ± 3 days of the WACE date (lag 0). Otherwise, the WACE cases are not related to the Ural blocking.

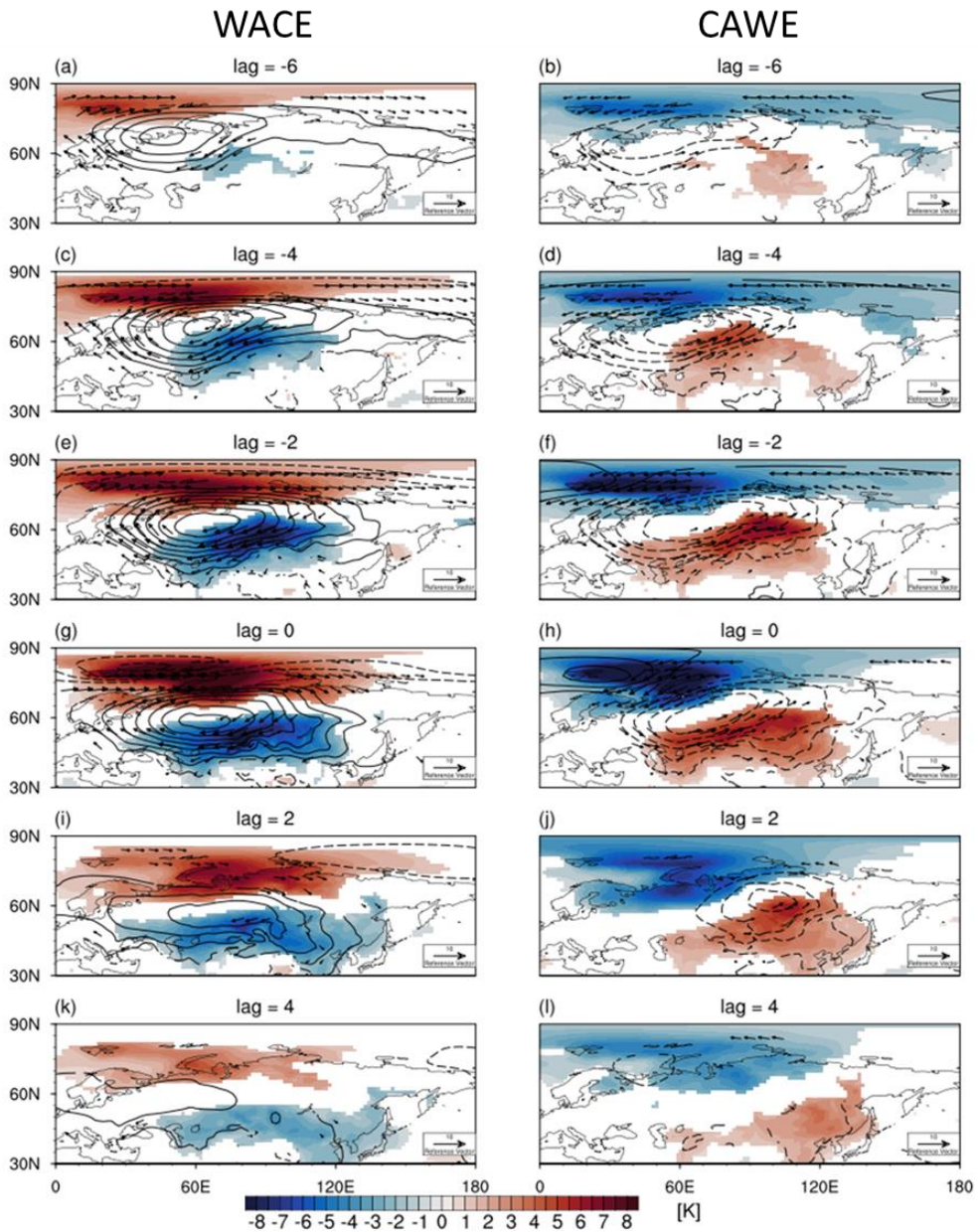


Figure 3.4. The lead-lag composite mean of SAT (shaded) and SLP (contour) anomalies and wind (vector) anomalies at 850 hPa for (left) WACE and (right) CAWE cases at lags (a-b) -6 days, (c-d) -4 days, (e-f) -2 days, (g-h) 0 days, (i-j) 2 days, and (k-l) 4 days with respect to the local maximum of DI. The contour interval for SLP anomalies is 2 hPa and the negative values are contoured in dashed line. Only the values that are statistically significant at the 95% confidence level are shaded.

It turns out that 78% of the WACE cases are accompanied with the Ural blocking which slowly moves westward in time (left column of Fig. 1.5). This result is consistent with the previous studies that suggest the Ural blocking as a key driver of the subseasonal WACE pattern (Luo et al. 2016b; Yao et al. 2017; Ye and Messori 2020). However, the other 22% are not directly related to the Ural blocking (right column in Fig. 1.5). They are instead associated with an eastward-moving anticyclone. The number of blocking and non-blocking WACE differs by the criteria (Table 3.1). When the WACE date (0 day) only considered as a blocking day, about 67% of WACE cases accompany Ural blocking.

Table 3.1. The number of blocking related WACE cases and the ratio to the entire WACE cases.

| criteria | number of cases | ratio (%) |
|-----------------|-----------------|-----------|
| 0 day | 52 | 67 |
| -3 day to 3 day | 61 | 78.21 |
| -5 day to 5 day | 65 | 83.33 |

This result indicates that the Ural blocking is not a necessary condition for the WACE pattern. A well-defined anticyclonic anomaly can result in the WACE pattern. It is noticeable that although the amplitude of SAT anomaly is comparable between the blocking and non-blocking WACE cases, the Ural blocking leads to more persistent anomaly in a broader region over the Eurasia. This implies that the Ural blocking is still an important factor in determining SAT anomalies (compare Fig. 1.5g and h).

The CAWE cases show a similar result to the WACE cases with an opposite sign (right column in Fig. 1.4). One distinctive difference from the WACE cases is the propagation of the Ural SLP anomaly. Unlike the quasi-stationary SLP anomaly of the WACE cases due to the mixture of the westward-moving Ural blocking and the eastward-moving transient anticyclone, the SLP anomaly of the CAWE cases migrates eastward through time. Its structure more resembles the SLP anomaly of the non-blocking WACE cases (right column in Fig. 1.5). This result indicates that the CAWE pattern is mainly determined by the transient cyclonic anomaly over the Ural region.

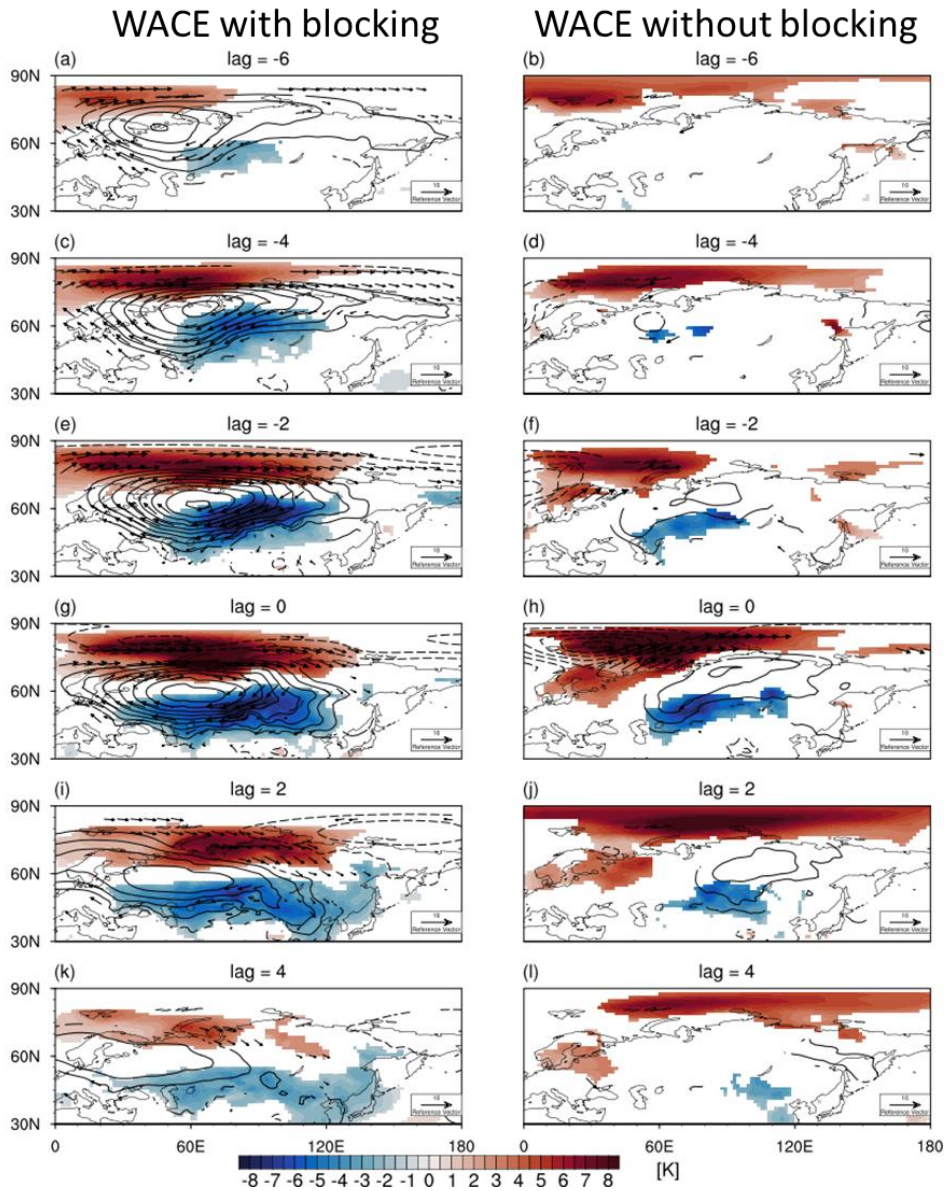


Figure 3.5. Same as Figure 3.4. but for (left) WACE with blocking and (right) without blocking cases.

To identify the physical processes that determine the WACE and CAWE patterns, temperature budget is computed at the 850-hPa pressure level (see section 1.3.3). The 850-hPa temperature (T850) is used here to minimize the topographic effect over the Eurasia. Figure 1.6a and b shows the spatial distribution of the SAT tendency, averaged from -5 to 0 day, for the WACE and CAWE cases. They are well captured by T850 tendency (Fig. 1.6c and d), justifying the use of T850 instead of SAT in temperature budget analysis (see also Fig. 1.7a and b).

For the WACE cases, the horizontal temperature advection (Fig. 1.6e) explains most of the temperature change over the BKS and Eurasia. The diabatic heating shows an opposite sign to the temperature advection (Fig. 1.6g). The adiabatic heating matches well with the SLP anomalies (Fig. 1.6i). Downward motion over the anticyclonic anomaly results in the adiabatic warming, while it also accompanies the adiabatic cooling in the northwest and southeast. Here it is important to note that both diabatic (Fig. 1.6g) and adiabatic heatings (Fig. 1.6i) cancel the advective warming over the BKS and cooling over the Eurasia. This result is in stark contrast to the previous studies which highlighted the role of the diabatic heating especially the downward longwave radiation (Yao et al. 2017; Ye and Messori 2020).

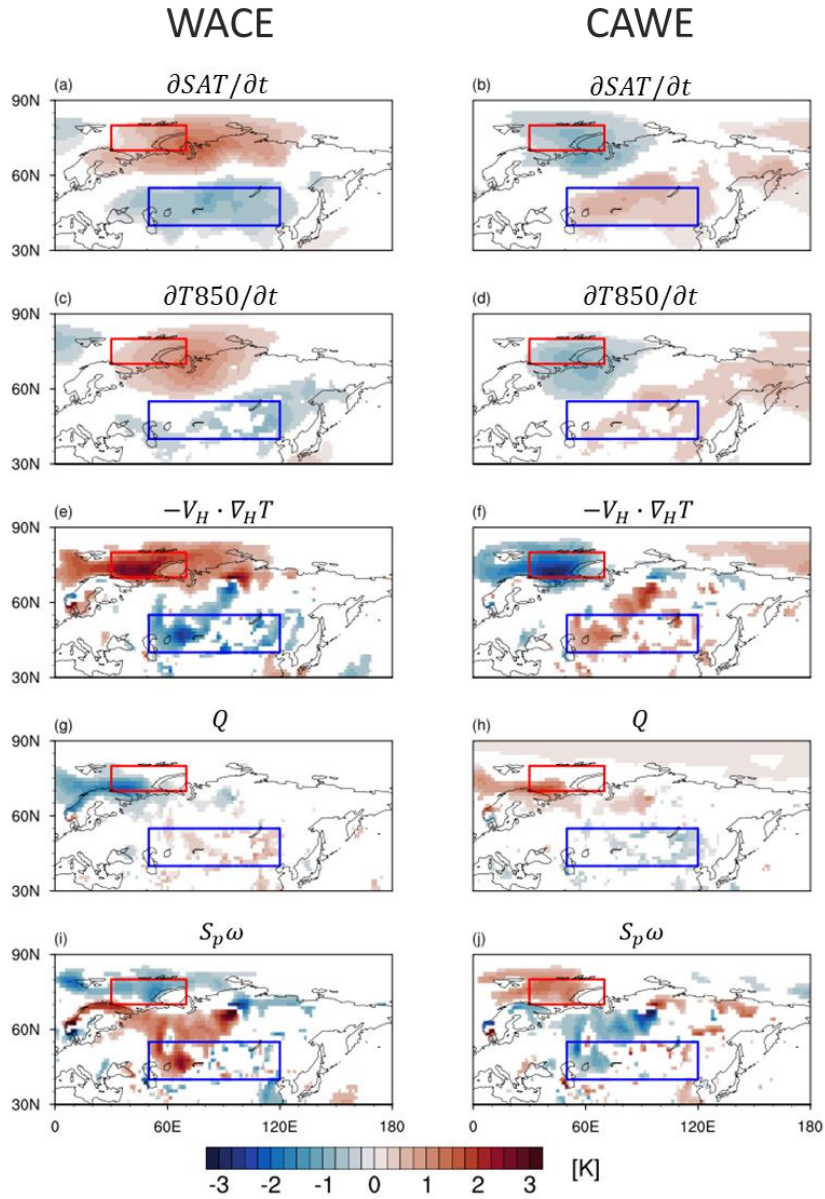


Figure 1.6. (a-b) The SAT tendency, (c-d) T850 tendency, (e-f) horizontal temperature advection, (g-h) diabatic heating, (i-j) adiabatic heating averaged from -5 to 0 days for (left) WACE and (right) CAWE cases. Note that all values are slightly smoothed by applying a nine-point local smoothing once and the underground values are excluded. Only the values that are statistically significant at the 95% confidence level are shaded.

Figure 1.7c and e confirms the results presented in Fig. 1.6. They show the temporal evolution of BKS and Eurasia T850 anomalies during the growth (-10 to 0 days) and decay phases (0 to 10 days). As shown in Fig. 1.6, the horizontal temperature advection (green) dominates the BKS T850 tendency (Fig. 1.7c). Both diabatic (blue) and adiabatic heatings (red) cancel the advective warming. Before the WACE date (lag 0), net diabatic heating is negative, and this is statistically significant. The adiabatic cooling appears around lag 0 day, largely cancelling the temperature advection during the WACE date. A similar mechanism holds for the Eurasian T850 tendency (Fig. 1.7e) with a larger cancellation between the advective cooling and adiabatic warming.

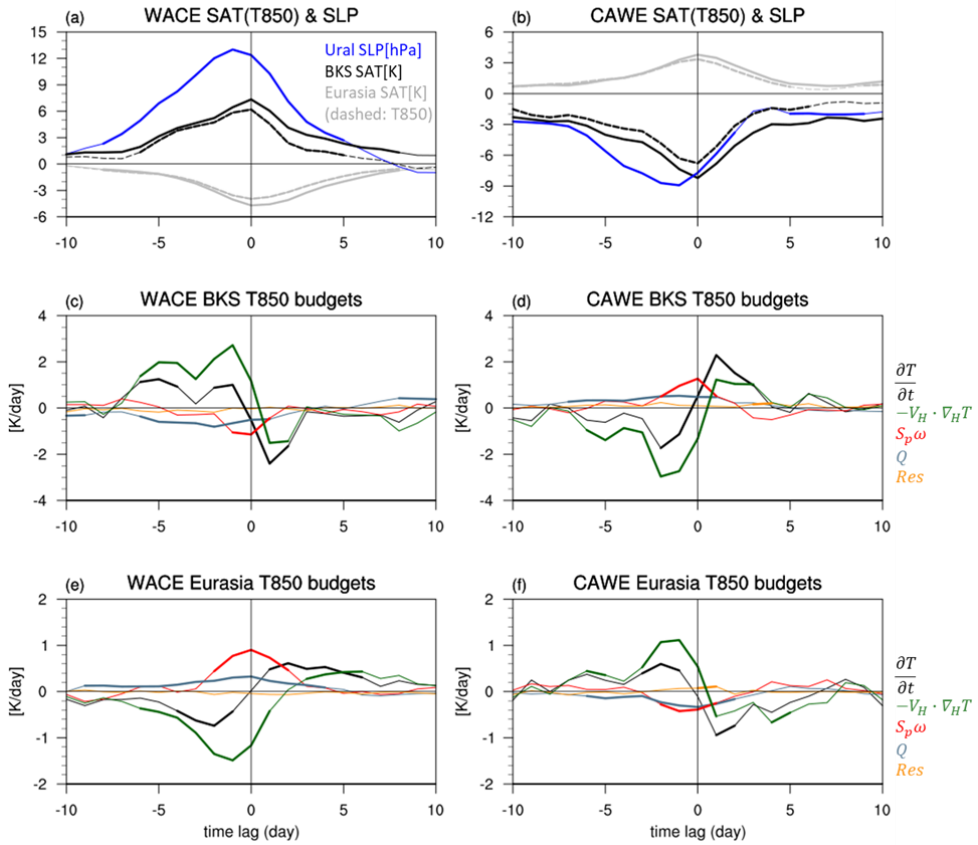


Figure 1.7. (a) Time evolution of lead-lag composites of BK (black) and Eurasian (gray) SAT (solid line) and T850 (dashed line) and Ural SLP (blue) for the WACE cases. Lead-lag composites of temperature tendency and budget terms in (c) BK seas and (e) Eurasia. (b,d,f) Same as in (a,c,e) but for CAWE cases. The statistically significant values at the 95% confidence level are bolded.

The same analysis is also conducted for the WACE cases with and without blocking (Fig. 1.8). As shown in Fig. 1.4, the amplitude of SAT anomalies over BKS is comparable although the Eurasian SAT and Ural SLP anomalies of the blocking WACE cases are much stronger (Fig. 1.8a and b). This result may imply that temperature anomaly over BKS is only weakly dependent on the presence of the Ural blocking while the Eurasian cold temperature anomaly is strongly influenced by the Ural blocking. It is further found that regardless of the presence of blocking, the temperature advection is the primary process that drives the WACE pattern. Figures 1.8b, d, and f show the T850 budget for the CAWE cases. Overall results are consistent with the WACE cases. It is concluded that both WACE and CAWE cases are mainly driven by the horizontal temperature advection.

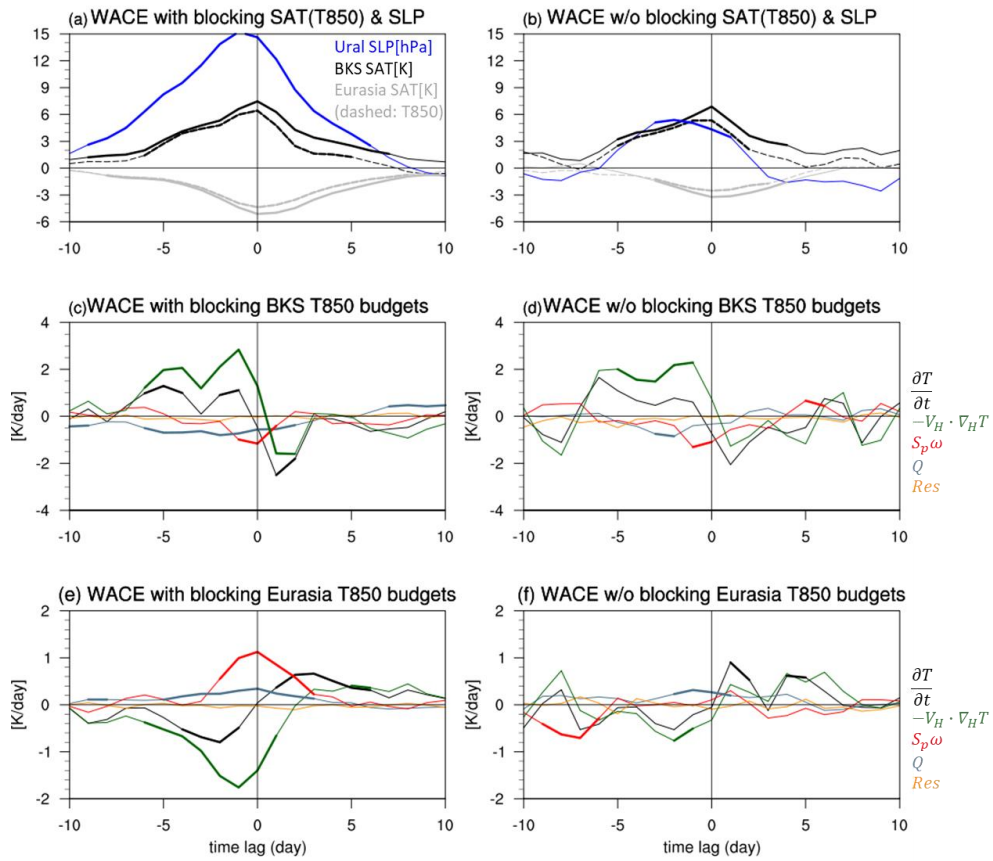


Figure 1.8. same as Figure 1.7 but for WACE cases with and without blocking.

To examine the sensitivity of the result to the choice of the pressure level, the temperature budget at 850 hPa integrated from lag -5 to 0 days is further compared to that at 925 hPa (Fig. 1.9). The diabatic heating is recalculated as a residue by subtracting the all terms from the temperature tendency. This allows to mask the missing values over the complex terrain in Eurasia. A small residue in Fig. 1.7 justifies this approach. During the WACE growth phase from -lag 5 to 0 days, the mechanism holds at both 850 and 925 hPa (Fig. 1.9a and c). Although the diabatic heating becomes stronger near the surface (e.g. for BKS, -4.5K at 850hPa to -10.0K at 925 hPa), while the horizontal advection also becomes stronger (e.g. for BKS, 11.2K at 850hPa to 16.7K at 925 hPa). They are effectively cancelled out. The same result is also found for the CAWE cases (Fig. 1.9b and d).

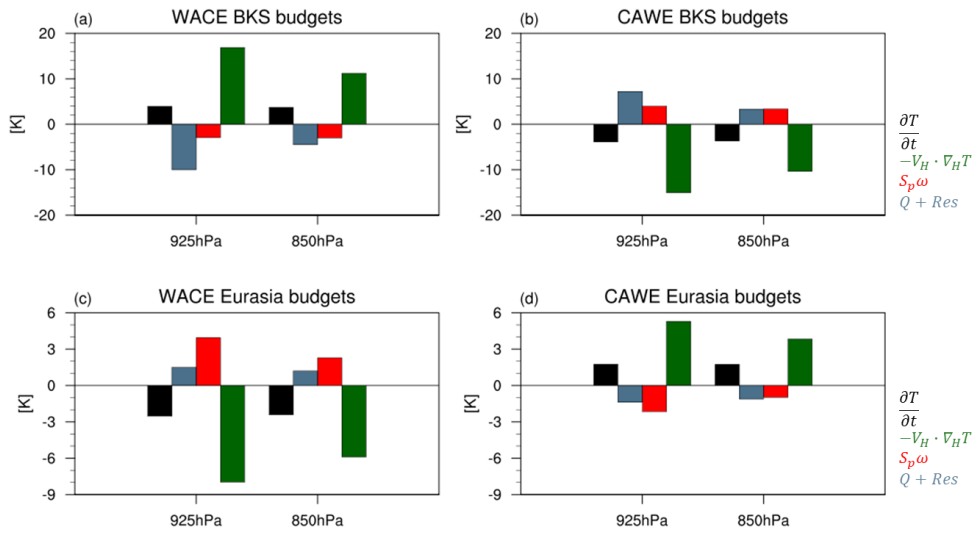


Figure 1.9. The time-integrated temperature tendency and budget terms for lag -5 to 0 days over (a-b) BKS and (c-d) Eurasia for (left) WACE and (right) CAWE cases.

1.4.3. Seasonality of the subseasonal co-variability

The remaining question here is why the seesaw-like BKS-Eurasian SAT variability is absent in summer. The SLP anomaly over the Ural region exists in all seasons, possibly exciting dipolar SAT anomalies even in summer. The Ural high (not necessarily blocking) cases in winter (NDJF) and summer (June to August; JJA) are compared in Fig. 1.10. The sampling method is identical to the WACE and CAWE samplings, but the time series of Ural SLP anomaly is utilized as a reference. Figure 1.10 illustrates the composite SAT anomalies and T850 climatology when the Ural SLP is anomalously high. In winter, SAT anomalies exhibit the WACE-like north-south dipole pattern. However, those in summer show the west-east dipole pattern that is not well projected onto the WACE pattern. This difference is due to the background temperature distribution. In summer, climatological temperature has a zonally-symmetric distribution over the Eurasian continent (T850 contours in Fig. 1.10b). This allows only meridional temperature advection, resulting in the dipolar SAT anomalies in western and central Eurasia. However, in winter, cold temperature is centered over Siberia due to the Siberia High (T850 contours in Fig. 1.10a). This allows both zonal and meridional temperature advectations over the central Eurasia.

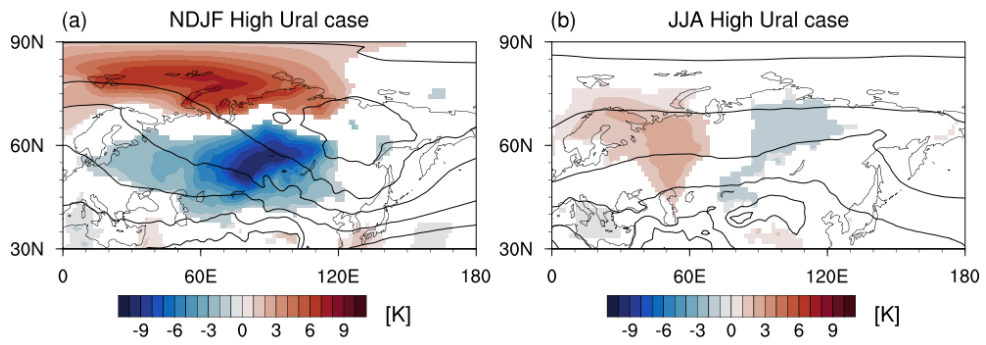


Figure 1.10. The composite mean of SAT anomalies (shaded) and T850 climatology (contour) for the high Ural SLP cases in (a) NDJF and (b) JJA. The contour interval for T850 climatology is 6K.

1.4.4. Subseasonal variability of the subseasonal co-variability

Figure 1.2 further reveals a bimodal distribution of SAT co-variability. It peaks in November and January with a local minimum in late December. This feature is also found in the regression coefficients of the Ural SLP anomaly (Fig. 1.3a and b), implying that the double peaks likely result from the circulation anomaly over the Ural region. The regression coefficient between the BKS and Eurasian SAT anomalies at lag 2 days (blue) and the standard deviation of the Ural SLP anomaly (black) are depicted in Fig. 1.11. for the same period. It becomes clear that the subseasonal variation of the BKS-Eurasian SAT co-variability is strongly influenced by the Ural SLP variability. This result highlights the crucial role of the weather systems over the Ural region in driving dipolar SAT anomalies between the BKS and Eurasia.

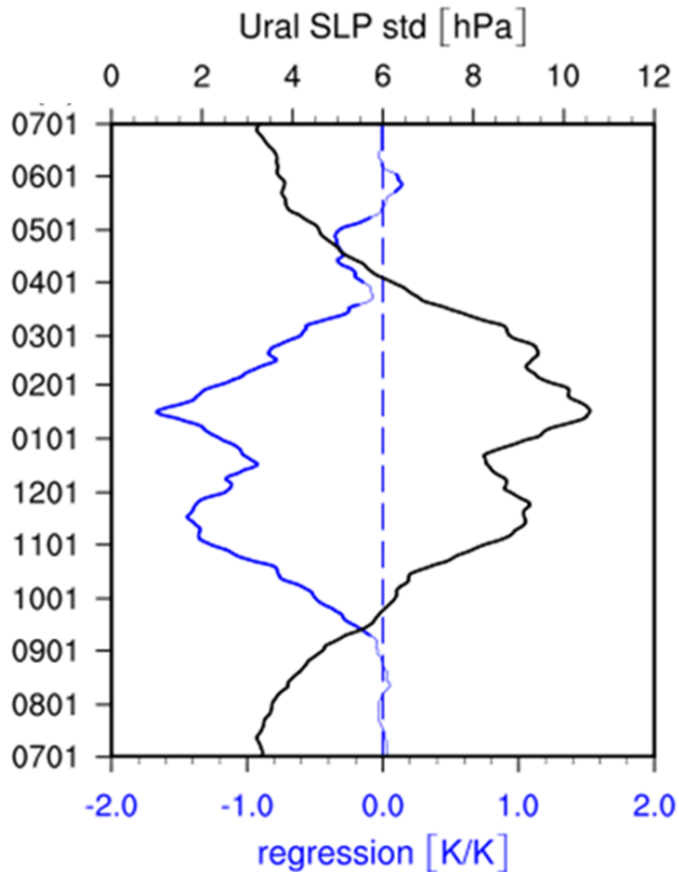


Figure 1.11. Regression coefficient (blue) at +2 days in Figure 3.2. and the standard deviation of Ural SLP anomalies. The y-axis is the starting day of the 30-day combined time series. Only the values that are statistically significant at the 95% confidence level are bolded in blue line.

To understand the bimodal distribution of the SLP activity, we construct the probability distribution function of the polar-cap averaged geopotential height anomaly at 50 hPa (Fig. 1.12) It turns out that the WACE cases in late winter are slightly biased to the negative geopotential height anomaly or weak polar vortex as in the interannual WACE cases. This bias is absent in the CAWE cases, indicating a subtle difference between the WACE and CAWE cases.

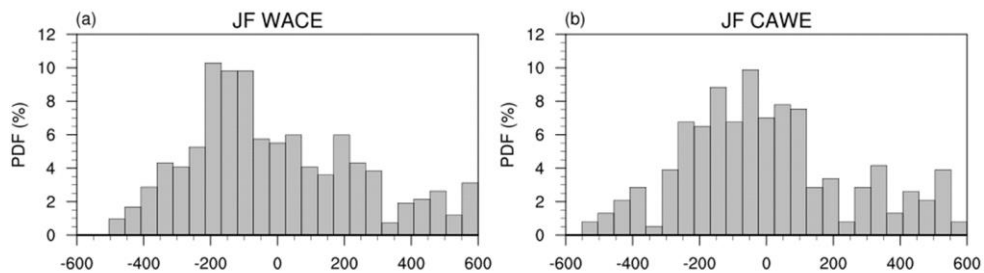


Figure 1.12. Histogram of polar cap (north of 65°N) averaged geopotential height anomaly at 50 hPa for (a) WACE and (b) CAWE cases in January and February. For each WACE or CAWE case, lag -3 to 3 days are considered to obtain the histogram.

1.4.5. Decadal variability of the subseasonal co-variability

The WACE and CAWE cases show different decadal variability. When the number of WACE and CAWE cases are counted before and after year 2000, the WACE cases increase from 1.55 to 2.44 cases per year. But the CAWE cases decrease from 2.65 to 0.89 cases per year (Fig. 1.13). This asymmetry is consistent with more frequent Ural blockings (Francis and Vavrus 2012; Yao et al. 2017; Tyrlis et al. 2020) and weakened Eurasian storm activities in the recent decade (Zhang et al. 2012; Wang et al. 2017). It was argued that the reduced meridional temperature gradient, resulting from the Arctic amplification, weakens the local baroclinicity and storm activities (Francis and Vavrus 2012; Tang et al. 2013; Yao et al. 2017; Wang et al. 2017). This provides a favorable condition for more persistent and stationary blockings (Yao et al. 2017; Luo et al. 2017; Luo et al. 2018), increasing the possibility of more frequent WACE cases. This result suggests that although the daily BKS-Eurasian SAT co-variability is a natural feature, the ratio of the WACE cases to the CAWE cases has changed (and will change) with time in response to the Arctic amplification. To better understand such change, the decadal variability of the WACE and CAWE cases in climate models warrants further investigation.

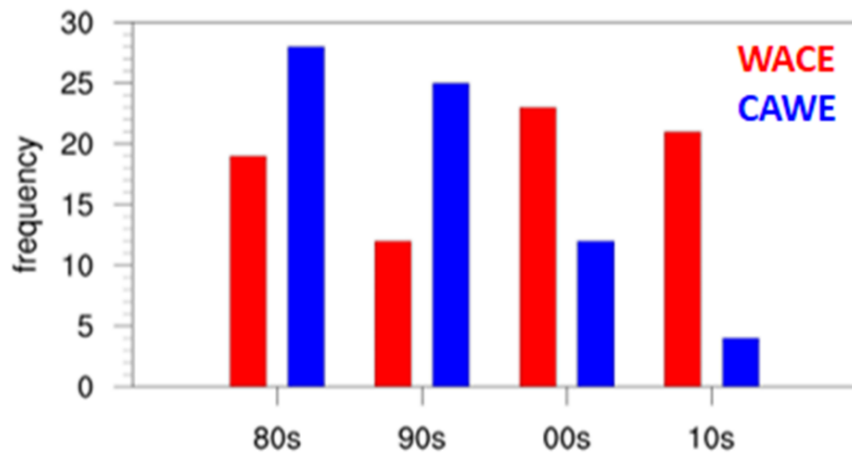


Figure 3.13. Frequency of the WACE (red) and CAWE (blue) cases during 1980 to 2017. Note that the last decade indicates the frequency of WACE and CAWE for 8 years of 2010-2017.

2. Interannual and long-term trend relationship of Arctic and Eurasia

2.1. Introduction

A negative trend of surface air temperature (SAT) has been observed over central and eastern Eurasia in boreal winter from the late 1990s to the early 2010s when Arctic sea ice extent has been rapidly declining (Cohen et al. 2014; Mori et al. 2014; Kim and Son 2020). This cooling trend played a key role in determining the strength of the global warming hiatus in the early 2000s (Deser et al. 2017). Statistical analyses of observational and reanalysis datasets have consistently demonstrated that Eurasian winter SAT is closely related to Arctic warming, especially sea ice loss over the Barents–Kara Seas (BKS), on both the interannual and decadal time scales (Francis and Vavrus 2015; Overland et al., 2015; Kim and Son 2020). For instance, the dipole pattern of the SAT anomaly, namely the WACE pattern, appears to be one of the leading modes of wintertime SAT variability on the interannual time scales and this mode is significantly correlated with the BKS sea ice change (Mori et al. 2014; Kim and Son 2016; Kim and Son 2020).

Numerous modeling studies have been conducted to verify the causal relationship between Arctic sea ice loss and Eurasian cooling (e.g., Mori et al. 2014; Cohen et al. 2014; Screen et al. 2018; Cohen et al. 2020). It has been revealed that the Eurasian SAT response to Arctic sea ice loss is generally weaker in climate models than the observations. Some models, especially those

with fully resolved stratosphere (Nakamura et al. 2016; Zhang et al. 2018), qualitatively reproduce the Eurasian SAT change, while others don't. The recent studies instead suggest that atmospheric internal variability is likely to play a critical role in driving both Arctic and Eurasian SAT changes (Screen et al. 2018; Xu et al. 2019; Blackport et al. 2019; He et al. 2020; Labe et al. 2020). He et al. (2020) showed that Arctic warming extending to the mid-troposphere is crucial to simulate the WACE pattern by examining historical simulations from Coupled Model Intercomparison Project Phase 5 (CMIP5). Labe et al. (2020) argued that this so-called "deep Arctic warming" or "full Arctic amplification", rather than surface warming driven by Arctic sea surface temperature (SST) and sea ice changes, was linked to an equatorward shift of the eddy-driven jet and Eurasian cooling.

The aforementioned studies, however, mainly focus on the interannual WACE relationship, which is not necessarily applicable to long-term trend relationship (e.g., McCusker et al. 2016). It has been well documented that, although most climate models can successfully reproduce the WACE pattern on the interannual time scale, the long-term WACE trend that appears in observations is not evident in these models (McCusker et al. 2016; Ogawa et al. 2018). Modeling studies with atmosphere-only models, for example, in which Arctic SST and sea ice concentrations were prescribed, showed no clear evidence of Arctic surface climate change that impacted the Eurasian SAT trend (Li et al. 2015; McCusker et al. 2016; Sun et al. 2016; Ogawa et al. 2018). A recent study using an atmosphere–ocean coupled model, in which the observed Arctic sea ice concentration was nudged, revealed a weak influence of Arctic warming

on mid-latitude circulation and SAT trends (Sun et al. 2018). However, as this study utilized only five ensembles, the results were questionable. More ensemble members are required to better quantify the impact of the declining Arctic sea ice on the long-term WACE trend more effectively.

To update and extend these studies, the present study quantifies the statistical relationship between the Arctic SIC and Eurasian winter SAT by using observation and revisits the possible impact of the Arctic sea ice change on the Eurasian SAT using the climate model simulations. We first determine the year (or period) when the decadal trend change of Arctic SIC and Eurasian winter SAT begins. Specifically, the starting year of the Eurasian winter cooling is objectively identified by conducting a break-point analysis, and this result is compared with the timing of the abrupt decline in Arctic SIC. The interannual covariability of Arctic SIC and Eurasian SAT anomalies is also quantitatively evaluated using a maximum covariance analysis. This method aims to better quantify the optimal time lag between Arctic SIC and Eurasian winter SAT variability without removing their linear trends. The possible impact of Arctic SIC change on Eurasian winter cooling is also briefly discussed by decomposing the SAT trend into that linearly congruent trend with the Arctic SIC loss and others.

Finally, the present study revisits the possible impact of the declining Arctic sea ice on the Eurasian winter SAT trend in an atmosphere-ocean coupled model by incorporating large ensemble simulations, with a total of 35 ensemble members, using the Geophysical Fluid Dynamics Lab Climate Model

version 2.1 (GFDL-CM2.1; Delworth et al. 2006). A large ensemble enables more effective quantification of the impact of Arctic sea ice loss on the midlatitude circulation and SAT trends, specifically the WACE trend. By dividing the ensemble members into two groups, with and without Eurasian cooling, this study demonstrates that the vertical extent of a polar warming and the stratospheric warming could be crucial for driving the WACE-like SAT trend.

2.2. Data

To quantify the statistical lagged relationship, we use the in-situ observation for SIC and SAT. The monthly mean SIC data is obtained from the Nimbus-7 Scanning Multichannel Microwave Radiometer and the US Defense Meteorological Satellite Program Special Sensor Microwave/Imager-Special Sensor Microwave Imager Sounder Passive Microwave Data set, version 1 using the NASA Team sea-ice algorithm (<https://nsidc.org/data/NSIDC-0051>; Cavalieri et al. 1996). These data were originally generated from brightness temperature data in a polar stereographic projection with a 25-km horizontal resolution but are interpolated into latitude and longitude grids with a 1-degree resolution. Following previous studies, the Eurasian SAT is primarily related to the BKS SIC.

The monthly-mean observed SAT is obtained from the NASA's Goddard's Global Surface Temperature Analysis (GISTEMP) data set. These data combine the SAT from the Global Historical Climatology Network data set version 3 and the SST from the Extended Reconstructed Sea Surface Temperature (ERSST) data set version 3b (Hansen et al. 2010) for the period 1979-2014. The temperature anomalies, relative to the reference period of 1951-1980, are available in a 2-degree resolution. The regional domains are set to 35-60°N and 50-130°E for Eurasia and 25-50°N and 75-120°W for North America.

Note that the analysis period for break point analysis and MCA is set to 1979-2014, since the break-point analysis (see below) is sensitive to the analysis period. This is not a specific problem of the break-point analysis; rather, it is a common linear regression issue. To reduce unnecessary noise, it is important to properly set the starting and ending years. In this study, the starting year is set to 1979 to match the sea-ice data. However, in consideration of the anomalously warm Eurasian SATs in the winters of 2014/15 and 2015/16 winters, the ending year is set to 2014 (e.g., Blunden & Arndt 2016, 2017; Xu et al. 2018). As this study aims to identify the Eurasian SAT trend change that began when the Arctic sea ice abruptly started to decrease, the most recent few years are excluded in from the analysis.

For the long-term trend analysis, we use the reanalysis data to compare the climate model experiments. Daily and monthly atmospheric variables, such as SAT, SLP, zonal wind, and geopotential height, were obtained from the fifth-generation European Centre for Medium-range Weather Forecasts atmospheric reanalysis (ERA5; Hersbach et al. 2020) with a horizontal resolution of $1.5^{\circ} \times 1.5^{\circ}$. Their anomaly is defined as a deviation from the daily or monthly climatology over the period of 1986-2015; that is, the analysis period of the model simulation, as described below. Note that the analysis periods for break point analysis and the climate model simulations are not identical because of the model spin-up time.

2.3. Methodology

2.3.1. Break point analysis

One of the main goals of the present study is to detect the change in a linear trend. Many approaches have been proposed to incorporate trend change(s) in linear regression models. We adopt the regression model that allows only one time-break point in the linear trend (Perron and Yabu 2009; Estrada et al. 2013).

$$y(t) = \alpha t + \beta dt + y_0 + n(t) \quad (4)$$

$$dt = t - t_B \quad t > t_B \quad (5)$$

$$dt = 0 \quad t \leq t_B \quad (6)$$

Here, y and t denote the interest and time in years, respectively. The two coefficients, α and β , determine the first trend before the break point (t_B) and the second trend after the break point, respectively. The linear trend from $t = 1$ to $t = t_B$ is set by α , whereas the later trend from $t = t_B + 1$ to $t = t_{\max}$ is set by $\alpha + \beta$. Since the analyzed time period is 35 years, from 1979 to 2013, t_{\max} is 35. The last two terms in the equation, y_0 and $n(t)$, are the y intercept and the residual component, respectively. Note that Eq. (4) differs from a simple linear regression because of dt . This term, which is absent in a simple linear regression model, defines the break point in the linear trend.

The best estimate of the break year, t_B , is determined with the least squared error. With the initial guess of the break year t_B ranging from 1 to 35, the value that satisfies the minimum squared error between the observed time series and the two regressions fits from $t = 1$ to $t = t_B$ and from $t = t_B + 1$ to $t = t_{\max}$ is considered the best estimation. The uncertainty of the trend change is then evaluated by examining the confidence interval proposed by Chang and Perron (2016). Only when the 95% confidence interval does not cross either the start (1979) or the end years (2013) of the analyzed period is the detected break point believed to be physically or statistically meaningful. Otherwise, the time series is considered to have no trend change.

Before the break-point analysis is conducted, the stationarity of the time series that is required for the linear regression analysis (Fuller 1995) must be evaluated with the unit root test incorporating the break point (Kim and Perron 2009). Although not shown, it was found that both the SAT and SIC time series, averaged over the analysis domains, are stationary at a 1 % significance level. This implies that the area-averaged SAT and SIC time series are suitable for the regression analysis with a break point.

2.3.2. MCA analysis

To better understand the interannual covariability between the Arctic SIC and mid-latitude SAT, we also performed a MCA. The MCA is based on the singular value decomposition (SVD) of the covariance matrix of the two variables (Bretherton et al. 1992; Wallace et al. 1992). Only the eastern hemisphere is considered for both the Arctic SIC (0-180°E and 60-90°N) and extratropical SAT anomalies (0-180°E and 30-90°N), as in Mori et al. (2014). To find the optimal time lag, September to November (SON), October to December (OND), November to January (NDJ), and December to February (DJF) SIC anomalies are tested against DJF SAT anomalies.

Although detrended data are often used in the MCA, raw data are used in this study. Detrended data would be more useful than the raw data for isolating interannual covariability, only if the variables of interest have linear trends. As shown later in this paper, both the Arctic SIC and Eurasian SAT have nonlinear trends with a significant trend change in the late 1990s. This makes the use of detrended data questionable. The use of raw data also allows us to investigate whether the leading expansion coefficient (EC) time series (see below) can reproduce the observed break point.

The MCA is specifically conducted as follows. The $SAT(x, t)$ at a grid point x and time t and the $SIC(x, t + \tau)$ at time $t + \tau$ are expanded in the MCA.

$$SAT^*(x, t) = \sum_n^N A_n(x) a_n(t) \quad (7)$$

$$SIC^*(x, t + \tau) = \sum_n^N B_n(x) b_n(t + \tau) \quad (8)$$

where SAT^* and SIC^* denote SAT and SIC anomalies, respectively. The time series $a_n(t)$ and $b_n(t + \tau)$ are the n^{th} EC time series obtained from the projection of the n^{th} singular vectors $A_n(x)$ and $B_n(x)$, obtained by the SVD of the covariance matrix, onto their original data. Here, the singular vectors are normalized and nondimensionalized, but the ECs have the same dimension as the raw data. Because we are mainly interested in SIC-induced SAT changes, τ is set to zero to negative values (e.g., $\tau = -1$ for NDJ SIC versus DJF SAT anomalies). The homogeneous SIC map and the heterogeneous SAT map are constructed by projecting $SIC^*(x, t + \tau)$ and $SAT^*(x, t)$, respectively, onto $b_n(t + \tau)$ (Bretherton et al. 1992; Czaja and Frankignoul 2002). Before the projection, $b_n(t + \tau)$ is scaled to make the homogeneous and heterogeneous maps have the same dimensions as the input data.

There is no formal procedure to evaluate the statistical significance of a MCA. As such, an empirical significance test, based on the bootstrap method, is carried out, as in Czaja and Frankignoul (2002). The MCA is repeated with the original SIC data and the randomly resampled DJF SAT data. This resampling is

conducted 100 times. The statistical significance is then evaluated by considering two metrics: the squared covariance fraction (SCF), which is a ratio of the squared covariance of a first leading mode against the squared covariance of all others, and the correlation coefficient (CC) between the leading EC time series of the SAT and SIC datasets. The significance level is defined by the percentage of resamples with an SCF or CC value equal to or greater than the value being tested.

2.3.3. Decomposition of a linear trend

The SAT anomalies, after the break point, are further decomposed into linearly congruent components with the SIC anomalies averaged over the BKS (SIC^*_{BKS}) and residuals (Thomson et al. 2000). When the SIC^*_{BKS} time series is represented by the linear trend (α) and the residual $\epsilon_1(t)$,

$$SIC^*_{BKS}(t) = \alpha t + \epsilon_1(t) , \quad (9)$$

the SAT^* time series can be regressed against SIC^*_{BKS} , as below:

$$SAT^*(x, t) = \beta(x)SIC^*_{BKS}(t) + \epsilon_2(x, t) = \alpha\beta(x)t + \epsilon_3(x, t), \quad (10)$$

where $\beta(x)$ is the regression coefficient of SAT^* onto SIC^*_{BKS} , and $\epsilon_2(x, t)$ is the residual in Eqn. 7. The coefficient $\alpha\beta(x)$ corresponds to the linear trend of SAT^* that is congruent with the SIC^*_{BKS} trend. The residual trend, i.e., the trend of ϵ_3 , is considered to be independent of the SIC^*_{BKS} trend. The linearly congruent trend is statistically significant only when both α and β are statistically significant.

2.3.4. Blocking index

A number of blocking detection algorithms have been applied in the literature (Dunn-Sigouin et al. 2013; Woolings et al. 2018; Hwang et al. 2020). The indices are largely grouped into anomaly, gradient-reversal, and mixed blocking indices. The mixed index, which combines the anomaly and gradient-reversal approaches, was employed in this study. Specifically, the MIX index described by Woolings et al. (2018) was used. Although not shown, it is noted that the overall results are not sensitive to the selection of the blocking index.

A blocking is detected from the daily geopotential height field at 500 hPa (Z500) over 45° to 80°N. A large anomaly is first detected when the Z500 anomaly is greater than the 90th percentile within three months. If this anomaly covers at least $2 \times 10^6 \text{ km}^2$ and satisfies a spatial overlap more than 50% within successive days for at least five days, it is classified as a blocking anomaly. It is ensured that this anomaly is accompanied by the gradient reversal, GR , as follows:

$$GR(\lambda, \phi) = \frac{Z500(\lambda, \phi: \phi + \Delta\phi) - Z500(\lambda, \phi: \phi - \Delta\phi)}{\Delta\phi} > 0$$

$$\phi_{max} - \Delta\phi/2 < \phi < \phi_{max} + \Delta\phi/2$$

where, λ and ϕ are the longitude and latitude, respectively, whereas ϕ_{max} and $\Delta\phi$ are the latitude of the maximum Z500 variance and detection window of 15°, respectively. See MIX index in Woolings et al. (2018) for further details.

2.4. Climate model simulations

The GFDL-CM2.1 was used in this study. This model is a fully coupled model consisting of atmosphere, land, ocean, and sea ice models. The atmosphere and land models have a horizontal resolution of approximately 2.5° longitude \times 2° latitude, while the ocean and sea ice models have a resolution of approximately $1^\circ \times 1^\circ$ in the tripolar grid. The vertical levels in the atmosphere and ocean were set to 26 and 50, respectively.

This model was forced by nudging the historical Arctic SST, north of 65°N , with a five-day relaxation time scale. The Extended Reconstructed Sea Surface Temperature (ERSST) v3b was used (Smith et al. 2008). All other forcings, such as greenhouse gases, anthropogenic aerosols and solar insolation, were fixed at the levels of the 1990s. A total of 35 ensemble members, with different initial conditions selected from the long-term equilibrium simulation, were conducted from 1951 to 2016. Among these, 15 members were identical to those used in Kim et al. (2020) whereas 20 members are newly added. Only the last 30 winters from 1986 to 2015 were analyzed in this study, with the first 35 years discarded as a spin-up period.

2.5. Results

2.5.1. Interannual and long-term trend relationship of Arctic and Eurasian SAT

Figure 2.1a-c presents the SAT time series and their linear trends in the NH extratropics, Eurasia and North America for summer (June-August; JJA) and winter (December-February; DJF). Not surprisingly, the NH-extratropical SAT has steadily increased from 1979 to 2014 in both seasons. However, the regional SAT trends have markedly different characteristics between seasons. In JJA, both the Eurasian and North American SATs show steady warming trends, with relatively weak interannual variabilities (red lines in Fig. 2.1b, c). In contrast, the DJF SATs show abrupt trend changes in the late 1990s with large variabilities (blue lines in Fig. 2.1b, c).

The break-point analysis revealed that the Eurasian and North American DJF SAT trends significantly changed in the late 1990s (Fig. 2.1b, c). The break point was particularly prominent in 1998. Note that although the detected year, 1998, has been empirically used in the literature (e.g., Kaufmann et al. 2011; Li et al. 2015), it is objectively identified as a break-point year in this study. Notably, the detected year is somewhat sensitive to the choice of the analysis domain. With varying domain size, the break-point changes slightly but is still observed in the late 1990s (not shown). Importantly, as Fig. 2.1b and c show, that the break point is statistically significant as the confidence interval does not cross the start and end years of the analysed period. Although a weak

hint of the trend change is observed in the NH-extratropical SAT (Fig. 2.1a), this change is not significant. Likewise, the JJA SAT does not show any hint of the trend change.

Notably, the sign of both the Eurasian and North American SAT trends switched at the same time (e.g., year 1998 in Fig. 2.1b,c) with the different confidence intervals. This result raises at least two possibilities: (1) there was a NH circulation change that coherently affected both the Eurasian and North American SATs; or (2) two different physical processes, which independently affected the Eurasian and North American SATs, occurred by chance in the late 1990s.

This issue is briefly addressed by examining the spatial structure of the DJF SAT trends before and after 1998 (Fig. 2.1d,e). Before 1998, significant warming occurred in central to south-east Eurasia and the east coast of North America. A weak warming trend is also evident in northern Europe. In contrast, weak and insignificant cooling occurred at high latitudes, north of 60°N. These trends, i.e., the strong mid-latitude warming and weak Arctic cooling, basically flipped after 1998 (compare Fig. 2.1d and e). The Eurasian and North American warming trends were replaced by statistically significant cooling trends. Likewise, the Arctic warming became particularly strong especially over the Greenland and Barents seas.

Figure 2.1e further shows that the SAT trends over the North Pacific are statistically significant in the latter period. These trend patterns resemble the negative phase of the PDO (Bond et al. 2003) and are connected to the North

American cooling trend through a wave-like trend pattern. These results may suggest that the DJF SAT-trend change in 1998 was likely associated with not only rapid warming in the Arctic but also a phase change in the PDO. The role of the PDO has been extensively discussed in the literature, and it is now well accepted that North American SAT trend changes are influenced by PDO phase changes (Meehl et al. 2011; Kosaka and Xie 2013; Meehl et al. 2013). However, the PDO cannot directly change the Eurasian SAT trend, as Eurasia is located upstream of the PDO region (Kosaka and Xie 2013). Instead, Eurasian cooling is more closely associated with Arctic warming and related atmospheric circulation changes (Honda et al. 2009; Petoukhov and Semenov 2010; Mori et al. 2014; Peings and Magnusdottir 2014; Barnes and Screen 2015; Overland et al. 2015; Nakamura et al. 2016; Mori et al. 2019).

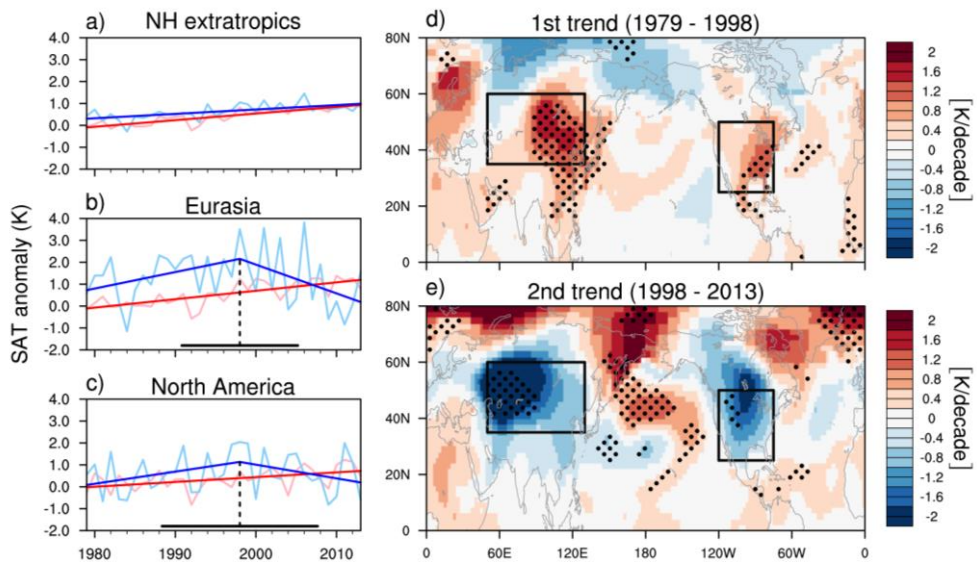


Figure 2.1. Area-mean SAT and its linear trend in DJF (blue) and JJA (red): (a) the Northern Hemisphere extratropics, (b) Eurasia and (c) North America. Dashed lines represent an extended trend in the absence of a breakpoint, and the black solid lines running parallel to the x-axis are the 95% confidence interval of the estimated break point indicated by the black dashed lines. The right column shows the DJF SAT trend (d) before and (e) after 1998. The values that are statistically significant at the 95% confidence level are dotted. Two boxes denote the Eurasian and North American domains.

Did Arctic sea-ice loss start at the same time (or period) as Eurasian winter cooling? To address the SIC–SAT trend relationship, a break-point analysis was also performed with the BKS SIC time series (Fig. 2.2). Notably, the BKS SICs in autumn and winter abruptly decreased in approximately 1998 (Fig. 2.2a-d), coincident with the timing of the Eurasian winter cooling (compare Fig. 2.1b and Fig. 2.2a-d). Unless they happened by chance, these results may suggest that the recent Eurasian cooling was partly associated with the BKS sea-ice loss.

Figure 2.2e-h illustrates the spatial pattern of the Arctic SIC trend since 1998. In autumn (SON), the SIC shows a significant negative trend over broad regions from the BKS to Chukchi seas (Fig. 2.2e). This negative trend is maintained in large areas of the Arctic ocean until the early winter (Fig. 2.2f,g) but is mainly restricted to the BKS seas in DJF (Fig. 2.2h). This result indicates that BK SIC loss is a robust heat source to the atmosphere from autumn to winter. However, it is difficult to determine whether the autumn SIC decrease (and the accumulated heat release from the ocean to the atmosphere until winter) is more important than the concurrent winter SIC change.

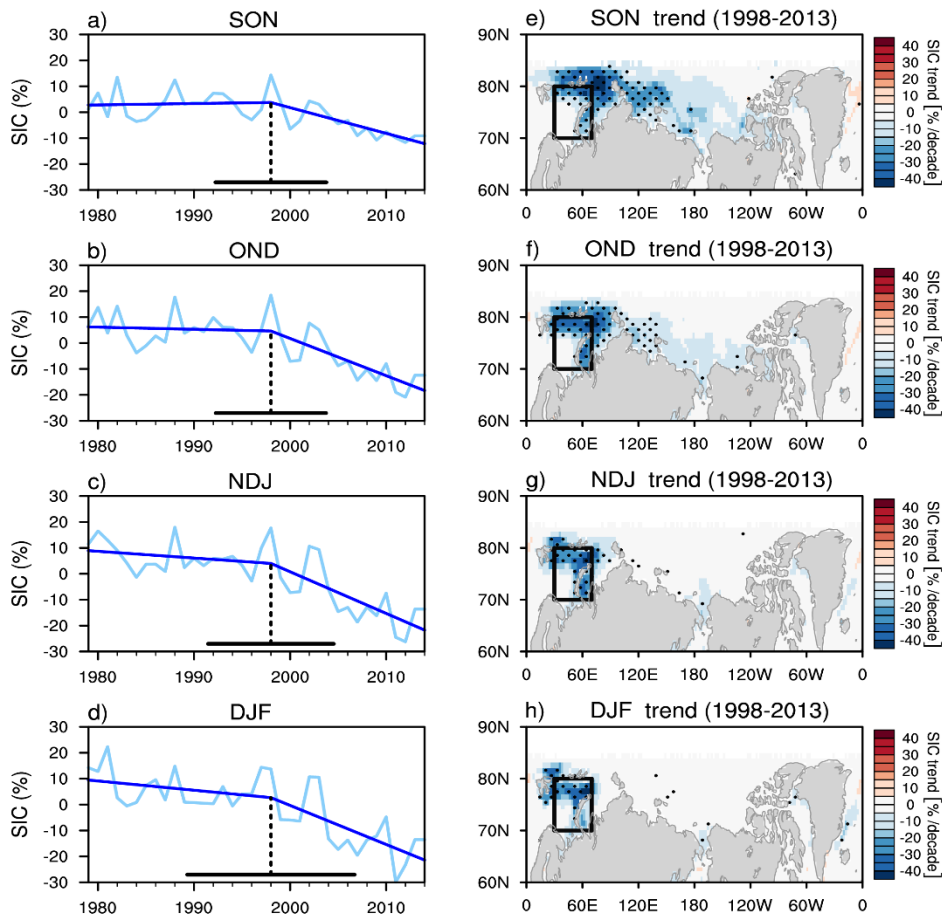


Figure 2.2. (a) SON, (b) OND, (c) NDJ, and (d) DJF SIC and their linear trends over the BKS. The overall format is identical to that of Fig. 2.1a. Right panels show the linear trend in SIC in each season since 1998. The values that are statistically significant at the 95% confidence level are dotted. The boxes in the right column denote the domain of BKS.

To identify the optimal time lag (or the absence of the time lag), the relationship between the Arctic SIC and Eurasian winter SAT anomalies is further quantified by MCA. The optimal time lag is determined with a maximum and statistically significant SCF. Note that although CC can be also used to define the lag, it does not allow a direct comparison among MCAs as each CC is computed with different EC time series. Table 2.1 summarizes the information explained by the leading mode obtained from the MCA. The SCF of the leading modes exceeds 70% and the CC is greater than 0.7 for all time lags. More specifically, the first leading mode accounts for approximately 50% of the SIC variance and approximately 25% of the SAT variance. This indicates that the MCA results are robust regardless of the SIC reference season. However, not all results are statistically significant. The first mode of DJF SAT against DJF SIC shows a 23% significance level, which is much larger than any others (see the last column of Table 2.1). This result suggests that the mid-latitude SAT anomalies lag behind the Arctic SIC anomalies by at least one month.

Table 2.1. SCF, CC, percent variances of SIC and SAT, and their significant levels explained by the first leading mode derived from the maximum covariance analysis (MCA) for SON to DJF SICs and DJF SAT.

| | SCF | CC | SIC | SAT | Sig. level |
|---------------------|-------|------|-------|-------|------------|
| SON SIC vs. DJF SAT | 83.07 | 0.74 | 48.14 | 25.59 | 3 |
| OND SIC vs. DJF SAT | 86.80 | 0.72 | 53.02 | 26.93 | 1 |
| NDJ SIC vs. DJF SAT | 78.63 | 0.74 | 54.19 | 23.29 | 10 |
| DJF SIC vs. DJF SAT | 72.36 | 0.85 | 54.21 | 20.47 | 23 |

Based on the maximum SCF and the MCA significance, the optimal covariability is found between the OND SIC and DJF SAT anomalies. The statistically significant CC in ECs in OND SIC and DJF SAT also implies that this mode well represents the association of winter SAT change with the autumn SIC change. Figure 2.3c and d illustrate the spatial and temporal structures of the leading mode of the OND SIC and DJF SAT anomalies, . These figures clearly showing the WACE-like pattern. More importantly, the resulting EC time series (Fig. 2.3a,b) are closely related to the BKS SIC (Fig. 2.2b) and Eurasian SAT time series (Fig. 2.1b). Their CCs are 0.94 for the SIC time series and 0.92 for the SAT time series. Both the interannual variability and the decadal trend change are well captured by the leading EC time series. Note that although the break point of the SAT EC time series appears in 2001, it is not significantly different from the observed break point in 1998, as the confidence interval overlaps. Essentially, the same result is also found when monthly data, instead of three-month-averaged data, are used (not shown).

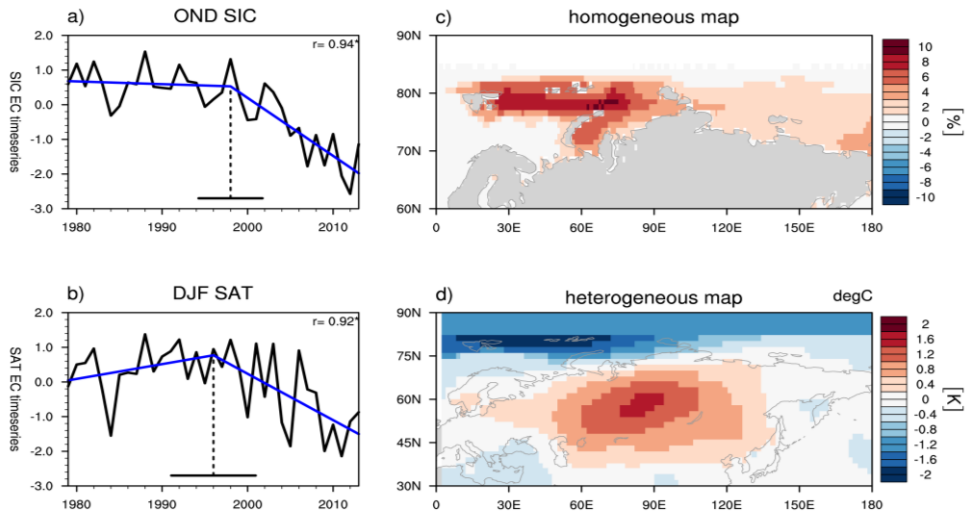


Figure 2.3. (left) EC time series of the leading mode of the MCA and their trends of the (a) OND SIC and (b) DJF SAT. The overall format is identical to that of Fig. 2.1a. The numbers in the top right corners of (a) and (b) denote the correlation coefficients with the Barents-Kara SIC time series (Fig. 2.2b) or the Eurasian SAT time series (Fig. 2.1b). The right column shows the (c) homogeneous (OND SIC projection onto the leading EC time series of OND SIC) and (d) heterogeneous (DJF SAT projection onto the leading EC time series of OND SIC) maps for 1979-2013. Note that the latitudinal domain of (c) is different from that of (d).

Here, we emphasize that the MCA results have at least two novel characteristics. (1) Because the SAT and SIC data in the Eastern Hemisphere, rather than those in a specified domain (e.g., Fig. 2.1), are used, the detected break points in Fig. 2.3a and 2.3b are free from the influence of the analysis domain choice and prove the presence of the WACE-like trend change in the late 1990s. (2) The optimal time lag between the SIC and SAT anomalies is identified to be approximately two months based on interannual to decadal time scales. Although this result does not guarantee causality, it suggests that Eurasian SAT anomalies and their trends are likely influenced by Arctic sea ice and related large-scale atmospheric circulations.

This lagged relationship can instead be explained by the stratospheric pathway. The key idea of this pathway is that the heat released by Arctic sea ice loss can generate vertically propagating waves that weaken the stratospheric polar vortex. The weakened polar vortex can then affect the troposphere in a manner similar to the tropospheric circulation change in response to stratospheric sudden warming (Jaiser et al. 2013; Cohen et al. 2014; Kim et al. 2014; Garcia-Serrano et al. 2015; Sun et al. 2015; Nakamura et al. 2016; Wu & Smith 2016; Zhang et al. 2018). The stratospheric pathway is examined by the heterogeneous regression map onto the EC time series of OND SIC (Fig. 2.4). The BKS warming induced by the sea ice loss causes the anomalous SLP near the BKS, and the associated vertical structure is stretched to the stratosphere. Figure 2.4 shows the lagged relationship with the OND SIC EC time series with the DJF circulation anomalies. Figure 2.5 further shows that the EC time series of OND SIC is more relevant to the DJF stratosphere than to the OND

stratosphere, implying that the Arctic sea ice loss is likely responsible for the changes in atmospheric vertical structure.

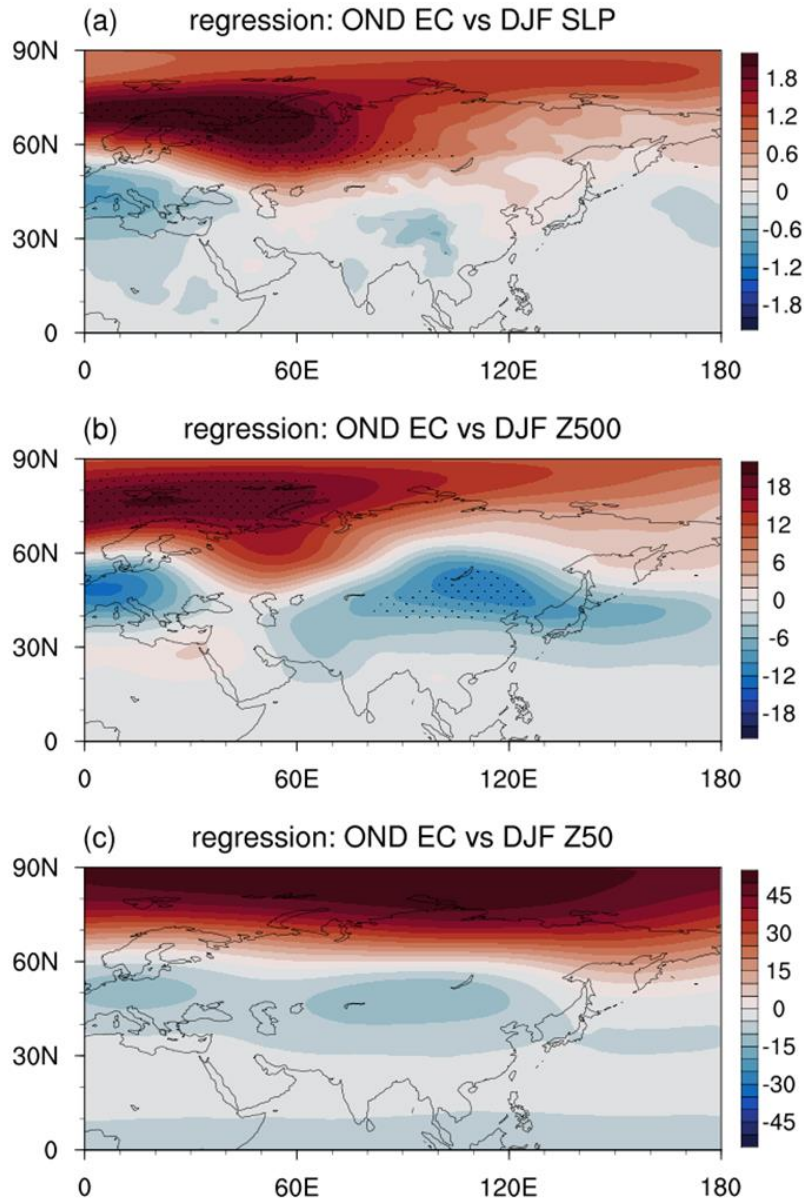


Figure 2.4. same as Figure 2.3(d) but for DJF (a) SLP, (b) Z500, and (c) Z50.

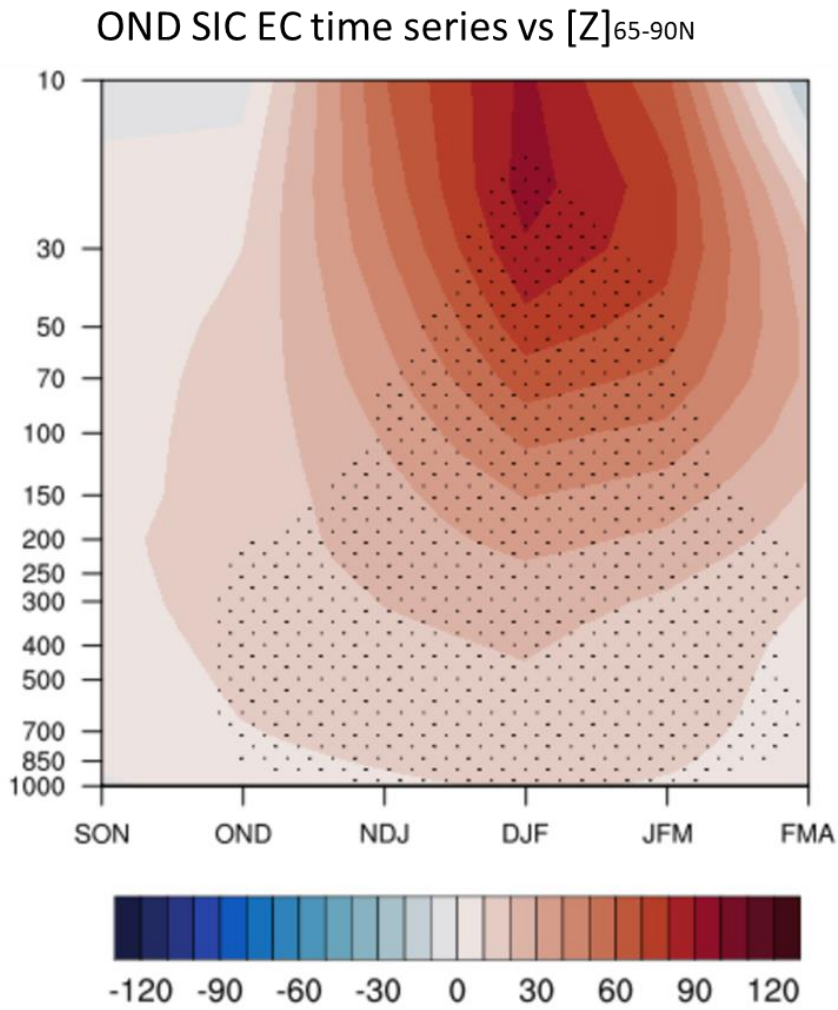


Figure 2.5. lead-lag regression map of PCI Z onto the leading EC time series of OND SIC for 1979-2013.

Although not shown, the second mode is also examined. The EC time series of SIC in this mode is not strongly correlated with the BK SIC time series ($r = 0.44$ in SON, $r = 0.18$ in OND, $r = 0.00$ in NDJ, and $r = 0.09$ in DJF). This indicates that the second mode does not represent BK SIC variability. Instead, the second mode is closely related to the AO index. The correlations between the second EC time series of the SAT and the AO index are 0.78 in OND, 0.82 in NDJ and 0.82 in DJF. These results complement those of Kim and Son (2016), who identified WACE as the first leading mode of the NH winter SAT variability, while the second leading mode is AO-related.

The possible impact of Arctic sea-ice loss on the SAT trend is further quantified by decomposing the SAT trend from 1998 to 2013 into a trend that is linearly congruent with the OND sea-ice loss and the leftover. The DJF SAT trend, which is linearly congruent with the OND BK SIC decrease, is presented in Fig. 2.6b. This trend resembles the DJF SAT trend very well (Fig. 2.6a), a result that again suggests that the Eurasian winter cooling since 1998 has at least partly been associated with the loss of autumn SIC over the BK seas.

It is noteworthy from Fig. 2.6b that the SAT cooling over North America is partly related to the BKS sea-ice loss. However, this cooling is unlikely to be directly associated with BKS sea-ice loss. As discussed in Screen (2017), North American SAT is more sensitive to sea-ice variability in the East Siberian–Laptev seas and Greenland Sea. Because Arctic sea-ice loss is not limited to the BKS but is observed to varying degrees in most Arctic Oceans, the North American cooling is likely associated with the overall Arctic sea-ice loss.

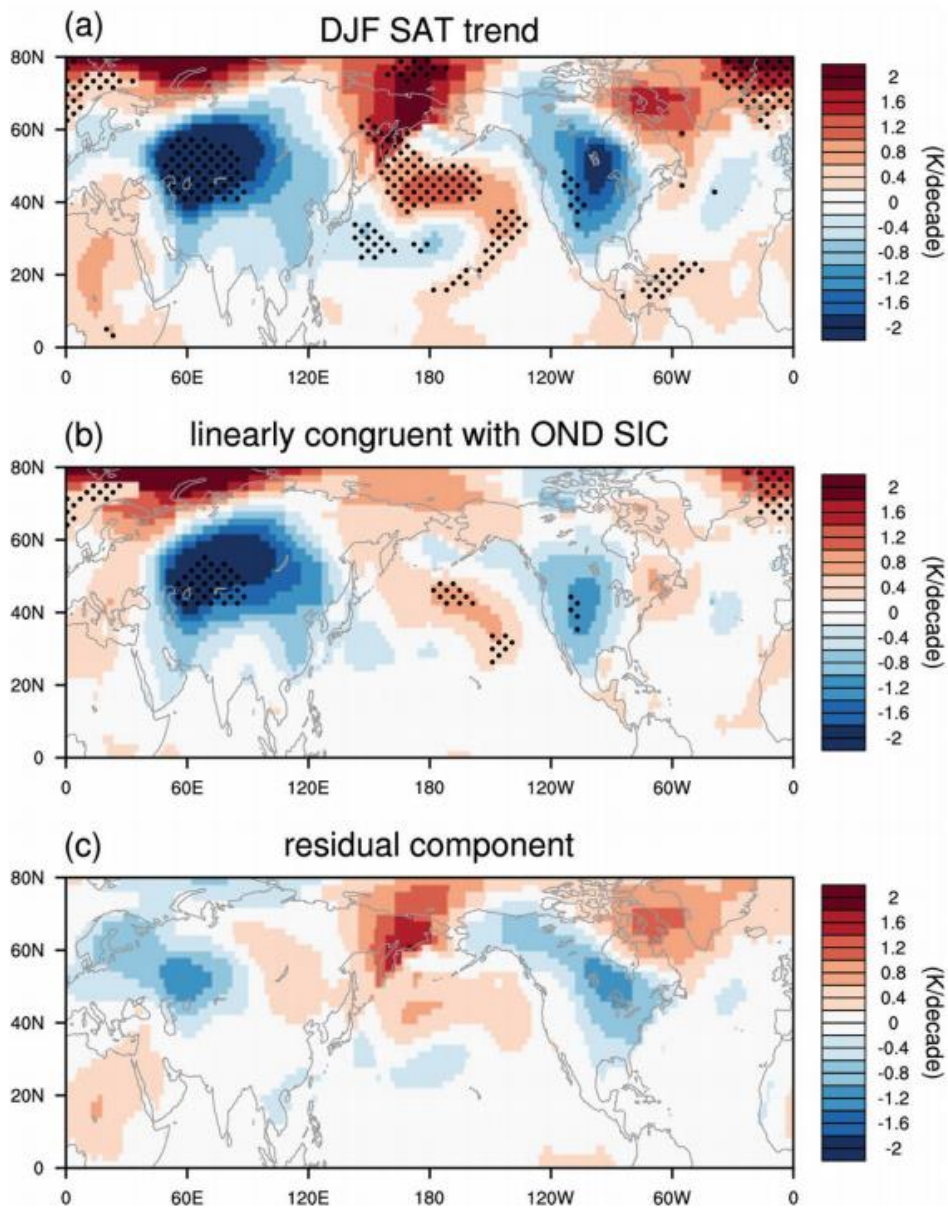


Figure 2.6. (a) Linear trend in the DJF SAT, (b) the trend that is linearly congruent with the OND SIC trend over the BKS seas, and (c) the residual component for 1998-2013. The values that are statistically significant at the 95% confidence level are dotted.

2.5.2. Polar restoring experiments in GFDL CM2.1

The stratospheric pathway, however, is not robust in climate models experiments. Even if a model that fully resolves the stratosphere, may fail to reproduce the WACE-like SAT response to Arctic sea-ice loss (Li et al. 2015). In such models, the WACE-like climate variability is not well reproduced (McCusker et al. 2016; Sun et al. 2016), making the stratospheric pathway questionable. Recent modelling studies have further argued that recent Eurasian winter cooling has simply been caused by natural variability (McCusker et al. 2016; Sun et al. 2016; Ogawa et al. 2018).

However, it is impatient to conclude that Arctic sea ice changes cannot be attributed to Eurasian SAT trend change, based on the results from the climate model experiments. One of the possible reasons is that the way to impose Arctic warming or sea ice loss in climate models differs (e.g. controlling the albedo, heat flux, sea ice concentration and sea ice thickness, etc., Screen et al. 2018). In addition, it was argued that an ensemble-mean response over the Eurasia could not be found when the number of ensemble members is less than 80 (Mori et al. 2014). Therefore, this study attempted to mimic the realistic sea ice reduction to simulate the Eurasian temperature trend change with enough ensemble members.

Figure 2.7. shows the observed and simulated seasonal cycle of SST and SIC over Arctic and BKS. For SST, in both Arctic and BKS, the overall seasonal cycles are well captured in climate model simulation (Fig. 2.7a,c). It is quite

obvious since the observed SST is nudged to the experiments. Then, the seasonal cycle of Arctic SIC, which is produced in the model by using the nudged SST is compared to the observation (Fig. 2.7b). The seasonal cycle of SIC tends to be consistent with the observation, while the seasonal variability is quite overestimated. The monthly mean SIC is less than observation when the sea ice decreases and is greater than observation when the sea ice is generated. This results imply that the seasonal variability of Arctic SIC seems to be comparable with the observation (Fig. 2.7b,d).

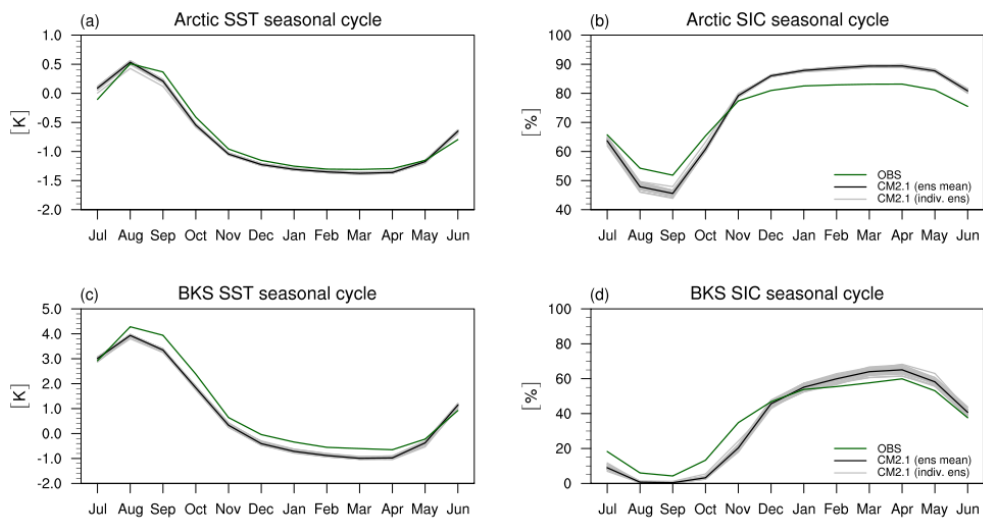


Figure 2.7. Seasonal cycle of Arctic (a) SST and (b) SIC in ERA-5 (green) and ensemble mean (black) and individual ensembles (gray) in CM2.1 polar restoring experiment. (c-d) same as in (a-b) but for BKS.

After removing their seasonal cycle, the interannual variability and decadal trend of SST and SIC over entire Arctic and BKS are examined (Fig. 2.8). The interannual variability of the annual mean Arctic SST in individual ensembles generally well matches to the observed SST. The ensemble-mean Arctic SST (black) is almost identical to the observation (green). This means that the interannual variability of the Arctic SST is well reflected in each experiments. Unlike annual mean Arctic SST, however, DJF Arctic SST time series in the individual ensemble members have different interannual variabilities (Fig. 2.8c). This may result in the nature of the coupled climate model, which generates the sea ice by applying the nudged SST, so that the open sea grid differs between each experiment and observations. The hypothesis is supported by the larger interannual variability of the SST over BKS, where the sea ice variability is the largest (Fig. 2.8e). For the SIC time series, the long-term negative trend follows the observed trend over both entire Arctic seas and BKS, while their interannual variability is sensitive to the ensemble members.

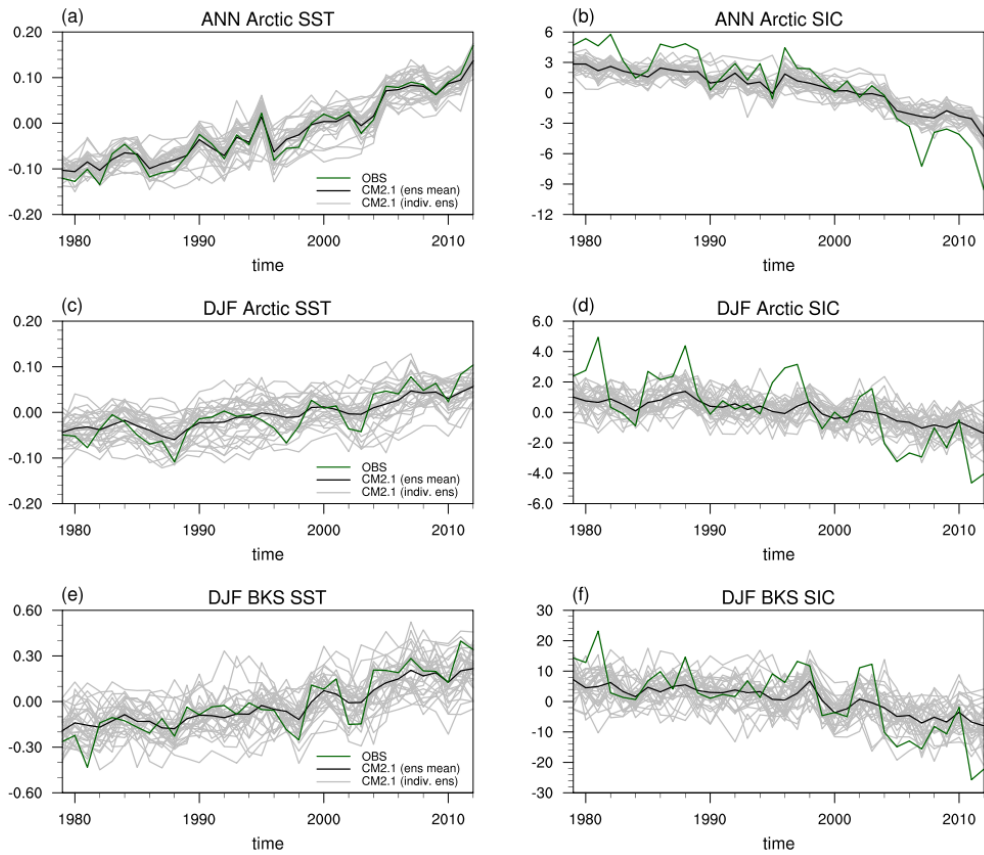


Figure 2.8. (a-b) Annual mean Arctic (70-90N) (a) SST and (b) SIC anomalies in ERA-5 (green) and ensemble mean (black) and individual ensembles (gray) in CM2.1 polar restoring experiment. (c-d) same as in (a-b) but for DJF season. (e-f) same as in (c-d) but for BKS.

2.5.3. Long-term trend in polar restoring experiments

Figure 2.9 shows the observed long-term trend of atmospheric variables, such as SAT, SLP, zonal wind at 300 hPa (U300), and blocking frequency, during 1986-2015 DJF. A strong warming trend is prevalent over the Arctic seas, while the cooling trend is found in central Eurasia (Fig. 2.9a). As mentioned above, this dipolar structure of SAT trends, known as WACE pattern, has been predominantly observed after the 2000s, concurrently with an abrupt sea ice loss in the preceding autumn and winter (Cohen et al. 2014; Kim and Son 2020; Ye and Messori 2020). As suggested in the previous studies (Francis and Vavrus 2012; Cohen et al. 2014; Xu et al. 2019), Arctic warming can induce anomalous large-scale atmospheric circulation at midlatitudes such as a high SLP anomaly in Siberia (Fig. 2.9b) through the weakening and eastward shift of the upper tropospheric jet stream (Fig. 2.9c). Under these conditions, blocking over the Ural Mountains occurs more frequently (Fig. 2.9d; see also Luo et al. 2016; Yao et al. 2017). Hence, both the southward cold air advection induced by the intensified Siberian High and a more occurrence of extreme cold days associated with an increased Ural blocking frequency result in the Eurasian cooling trends in the recent decades.

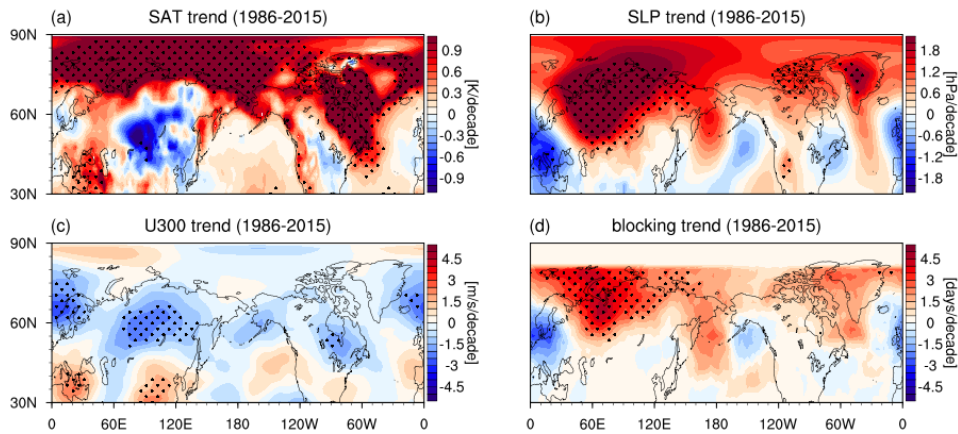


Figure 2.9. DJF-mean (a) SAT, (b) SLP, (c) U300, and (d) blocking frequency trend over the 1986-2015 from ERA5. Only the values that are statistically significant at the 95% confidence level are dotted.

Although the trends in Arctic sea ice loss and Eurasian winter cooling are concurrently found in the observations, there still be a discrepancy in the midlatitude responses among the climate model simulations (Li et al. 2015; McCusker et al. 2016; Sun et al. 2016; Ogawa et al. 2018). This is partly due to the opposite effects of tropics on the midlatitude jet, thus, the tropical upper tropospheric warming could lead to a poleward shift of the midlatitude jet while Arctic warming results in an equatorward shift of jet. This “tug-of-war paradigm” between the Arctic and tropics indicates that the historical all forcing simulations may not be suitable to understand the role of Arctic sea ice on midlatitude circulation changes. In this regard, the polar restoring experiments have been conducted in the present study to isolate the impact of Arctic warming associated with sea ice loss on the midlatitude atmospheric circulation without any consideration of radiative heating (see methods).

Figure 2.10 shows the long-term trend of atmospheric variables in the ensemble-mean (a total of 35 members) of coupled model simulations. A statistically significant SAT trend is confined only in Arctic seas, and its amplitude is much smaller than the observation. The ensemble-mean signal of SAT trends is not significant particular in Eurasia where the ensemble spread is larger than the other regions (not shown). This implies that the observed cooling trends in Eurasia through the modulation of atmospheric circulation (Fig. 2.9) are not likely due to the Arctic sea ice decline alone, as suggested by the previous studies (Li et al. 2015; McCusker et al. 2016; Sun et al. 2016; Ogawa et al. 2018). Not surprisingly, statistically significant changes in atmospheric circulation, which can alter Eurasian temperature, are not evident in the ensemble-mean trends (Figs. 2.10b-d).

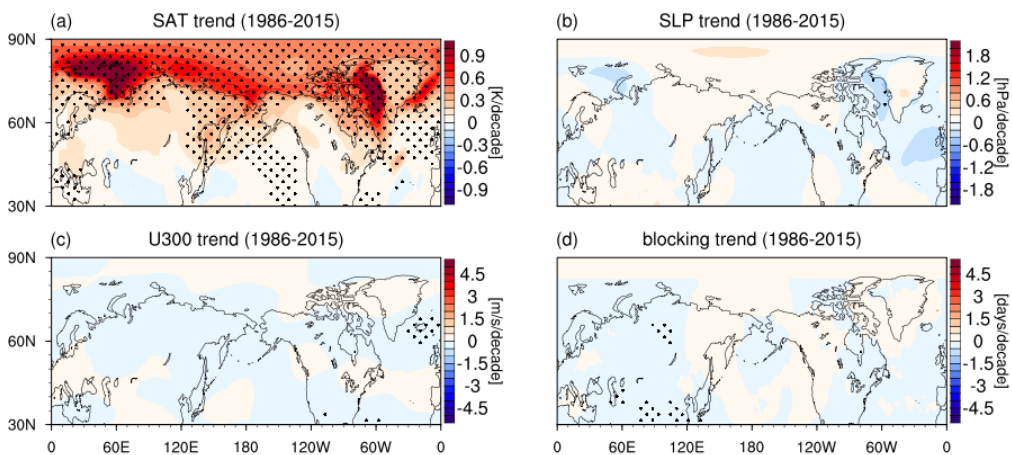


Figure 2.10. Same as Figure 2.9. but for the ensemble mean of 35 experiments in GFDL CM2.1.

To further estimate the ensemble spread of the changes in midlatitude atmospheric circulation, the area-averaged SLP trends over the Ural region (30-100°E and 50-70°N) are defined in individual ensemble members. Besides, their relationships to each corresponding trend in SATs over Eurasia (40-60°E and 50-130°N) and BKS (30-70°E and 70-80°N) are illustrated in Fig. 2.11 and 2.12. Only a half of the total ensemble members (17 of 35) shows a Eurasian cooling trend. For the relationship between Ural SLP and Eurasia SAT trends (Fig. 2.11), there is a strong inter-member correlation coefficient ($r=-0.82$) which value is statistically significant at the 95% confidence level. This result is consistent with the previous studies that they found the inter-member or inter-model relationship associated with internal atmospheric variability (McCusker et al. 2016; Sun et al. 2016). The individual BKS SAT trends, however, are not significantly related to each Ural SLP trend (Fig. 2.12). Although all ensemble members show a positive sign of BKS SAT trends, the Ural SLP trends have both positive and negative signs. These results confirm that the Eurasia SAT trends in each ensemble member are thermodynamically associated with the atmospheric circulations over the Ural region as in the observed long-term trends, but those circulations are not predominantly determined by the BKS SAT trends in the model.

Notably, although the previous studies have considered the observed Eurasian winter cooling as an extreme case outside the range between multi-model simulations (McCusker et al. 2016; Sun et al. 2016; Ogawa et al. 2018), our experiments suggest that the observed Eurasian cooling trend is within the range of ensemble spread. This result implies that the observed trend could be

one of the realizations produced by the internal variability without any other radiative heating. However, the observed Ural SLP and BKS SAT trends are slightly beyond the range of ensemble spread. Especially in BKS warming (y-axis in Fig. 2.12), the observed trend reaches 2.81 K per decade which value is almost 30% larger than the maximum value in the model experiments (2.1 K per decade). These results indicate that the recent BKS warming is not explained only by sea ice retreat (Labe et al. 2020; Cai et al. 2021). It hints that the other direct and indirect effect of radiative heating, which is not considered in our model experiments, may reinforce BKS warming.

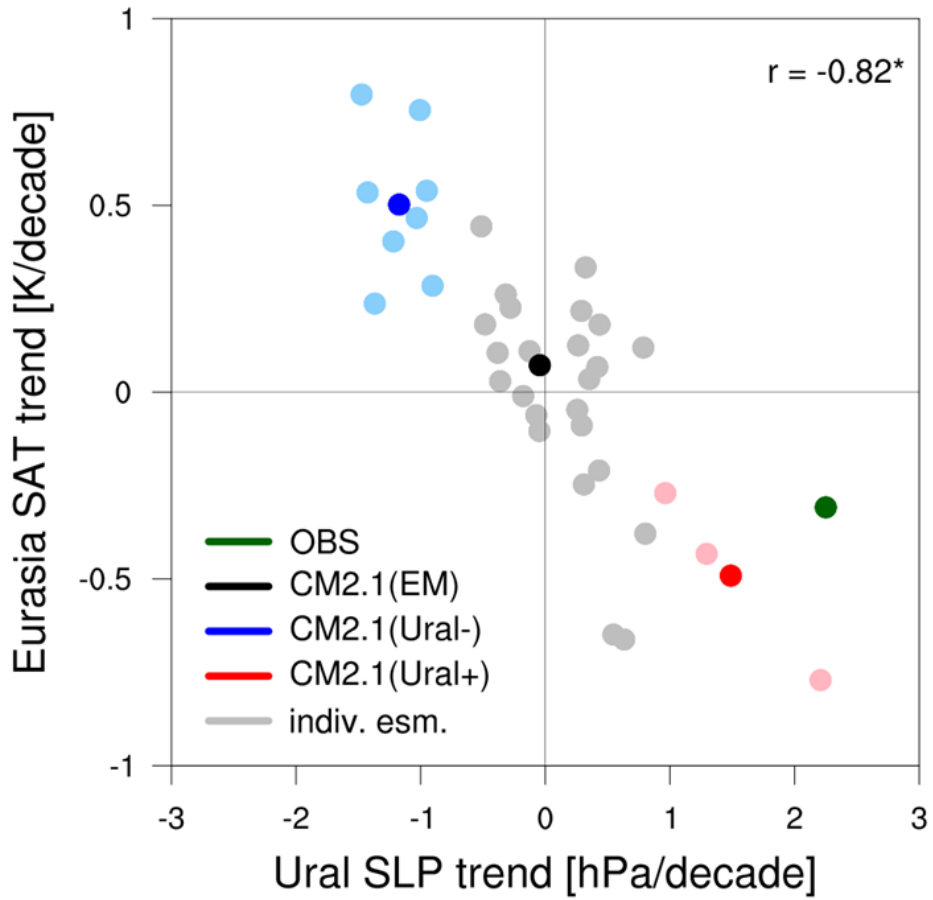


Figure 2.11. Relationship of the Ural SLP trend to Eurasian SAT trend in ERA5 (green) and the ensemble mean (black) and individual ensemble members (grey) in GFDL CM2.1 for the period of 1986-2015. Note that the ensemble members of Ural+ group are denoted in light pink, while that in Ural- group are denoted in light blue. The ensemble means of Ural+ and Ural- are denoted in red and blue, respectively.

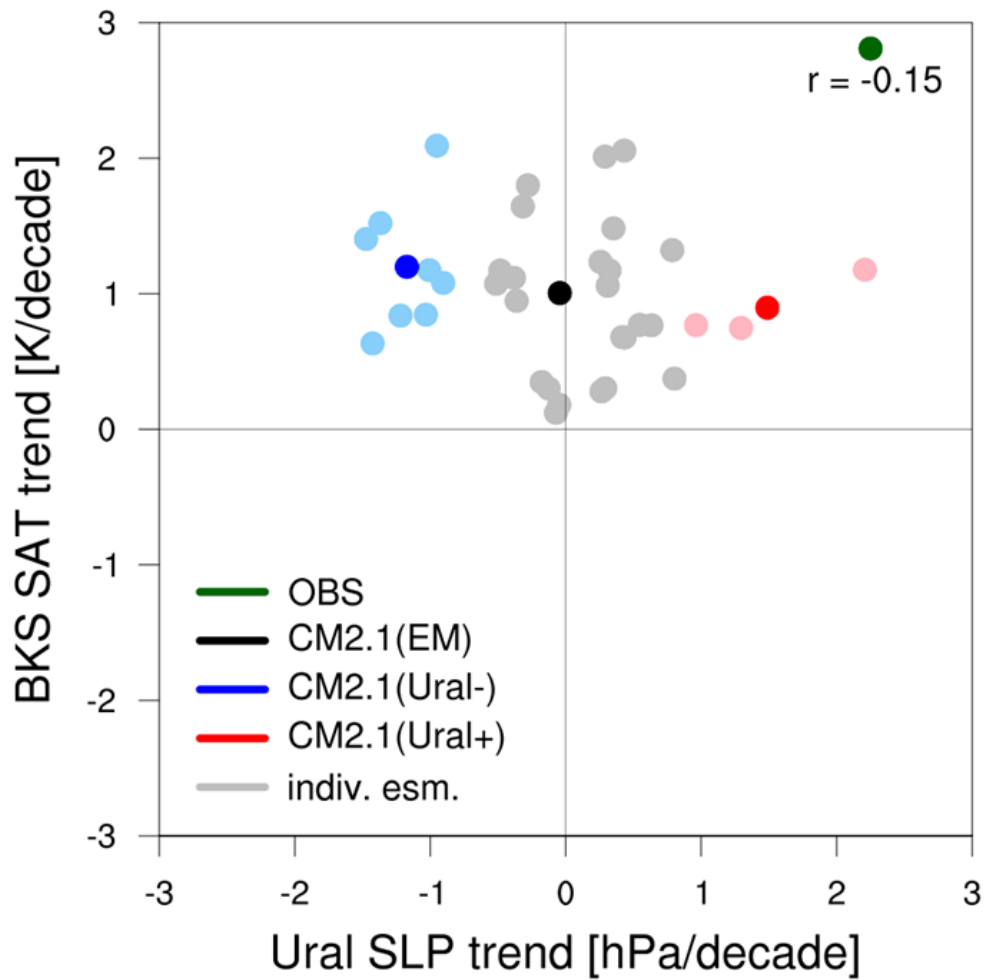


Figure 2.12. Same as Figure 2.11. but for BKS SAT trend.

To understand the critical role of internal variability on the trends in atmospheric circulation, we compare the extreme cases according to the sign of Ural SLP trends. Two groups – Ural High and Ural Low – are classified in which the Ural SLP trends exceed \pm one standard deviation of individual trends. Hence, the three ensemble members are included in Ural High cases, and the eight ensemble members are considered as Ural Low cases. Note that the ensemble means of Ural High and Ural Low cases have similar magnitudes of trends in BKS SAT.

The difference between the Ural High and the Ural Low cases is further investigated by comparing the composites of long-term trends (Fig. 2.13). The SAT and SLP trends in the Ural High cases represent quite similar patterns to the observed ones (compare Figs. 2.9a, b and Figs. 2.13a, c). In the Ural Low cases, however, the BKS warming tends to expand to the Eurasia region. Furthermore, although Arctic warming is found, a decreasing trend in SLP over the entire Arctic seas and its southward extension to the Ural region are evident (Fig. 2.13d). The substantial difference between two groups is also found in the trends of the tropospheric upper-level jet (Figs. 2.13e and f). A weakened and equatorward shifted jet stream corresponds to an anomalous surface high-pressure circulation in the Ural High cases (Figs. 2.13c and e). These atmospheric circulation changes with a barotropic structure located in the Ural region are also evident in the Ural Low cases but with an opposite sign (Figs. 2.13d and f). The long-term trends in the upper tropospheric jet stream are further linked with an increase and decrease in Ural blocking frequency in both groups, respectively (Figs. 2.13g and h). This result implies that Eurasian

cooling can occur under the Arctic warming conditions, only when the anomalous anticyclonic circulation exists in the Ural region accompanied by the weakening of upper tropospheric jet.

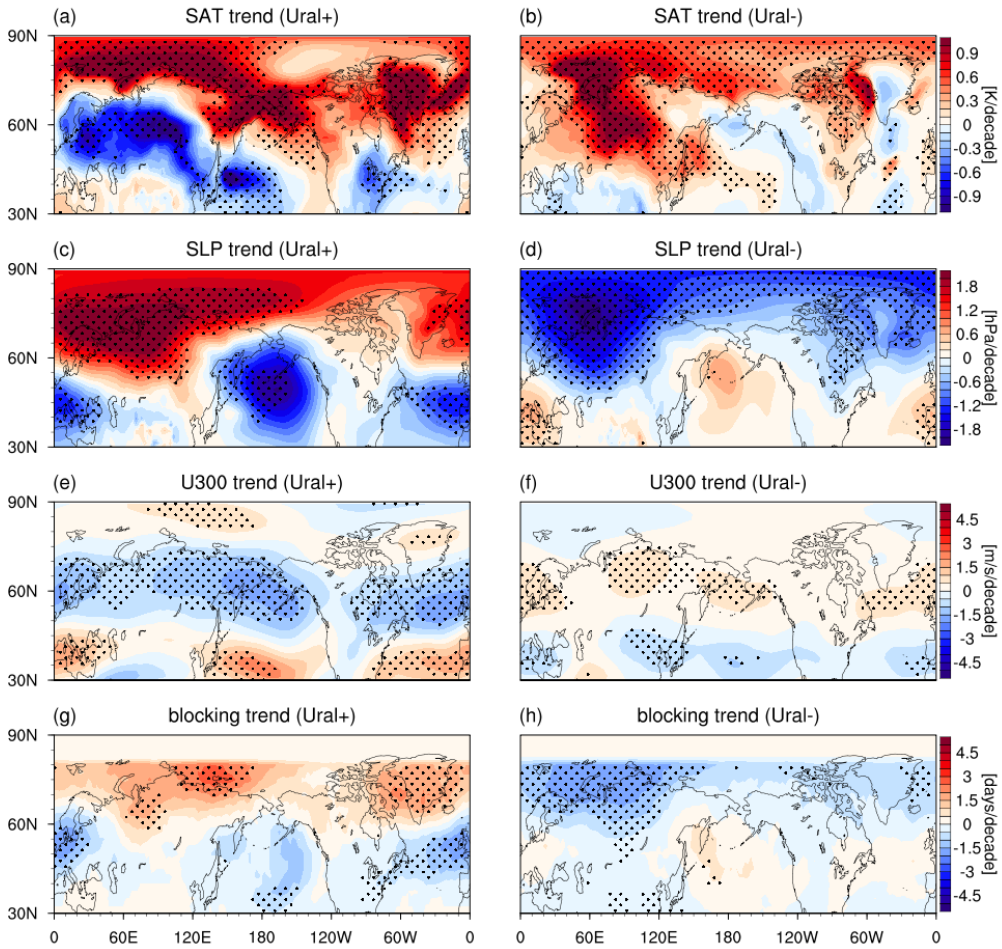


Figure 2.13. Same as Figure 2.10. but for ensemble means of (left) Ural+ group and (right) Ural- group.

The following question is what determines the circulation changes in the upper troposphere. To explain possible mechanisms for this question, the vertical structure of zonal-mean air temperature in both the Ural High and the Ural Low cases are investigated focusing on high-latitude (Fig. 2.14). Although the amplitude of Arctic surface warming near the BKS is similar in both cases (Fig. 2.14b), the vertical structures are quite different. For Ural High cases, the surface warming trend is well developed vertically, a statistically significant warming is found up to 400 hPa level (Fig. 2.14a). This deep Arctic warming tends to reduce the meridional temperature gradient in the upper troposphere. It is likely responsible for the weakening trends in upper-level jet, resulting in the anomalous anticyclonic circulation and increased blocking frequencies over the Ural region. However, in the Ural Low cases, Arctic warming is shallow and trapped in the lower layer below 850hPa even the cooling exhibits above 700 hPa level (Fig. 2.14b). This prevalent cooling trend in the upper troposphere increases the meridional temperature gradient, which induces an intensification of the upper tropospheric jet stream.

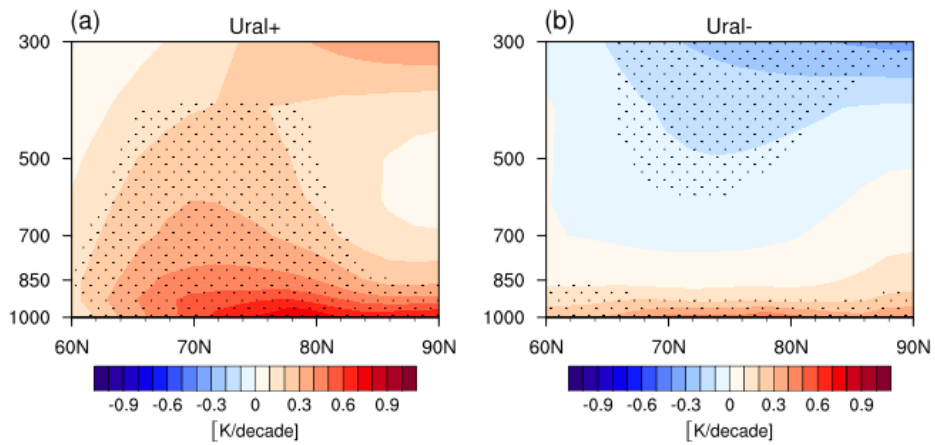


Figure 2.14. Vertical cross section of the zonally averaged DJF temperature trend over 1986-2015 in ensemble means of (a) Ural+ group and (b) Ural- group. Only the values that are statistically significant at the 95% confidence level are dotted.

The vertical structure of Arctic warming turns out to be an important factor for determining the atmospheric circulation change related to the Eurasian cooling trends. Thus, the linkage between the vertical extent of Arctic warming and the Ural SLP has been further investigated in individual ensembles (Fig. 2.15). To determine the indicator of the vertical extent of Arctic warming, we simply used the polar cap ($> 65^\circ\text{N}$) tropospheric temperature defined by vertically averaged air temperature from 700 to 300 hPa (PCI_T700-300hPa). It is found that there is a non-negligible linear relationship ($r=0.60$) between the trends in PCI_T700-300hPa and Ural SLP. It indicates that the Eurasian cooling is more pronounced as Arctic warming is deeper in the vertical. When Arctic warming is confined near the surface, however, the Eurasian SAT trend becomes even positive. It highlights the importance of the vertical structure of Arctic warming in simulating the Arctic-Eurasian climate co-variability.

This result is in agreement with the recent studies (Xu et al. 2019; He et al. 2020; Labe et al. 2020), they have suggested that the vertical distribution of Arctic warming can control the Eurasian temperature responses on interannual time scale. Although there are some hints for causes of deep Arctic warming, such as an increased atmospheric poleward energy transport due to remote SST changes (Screen et al. 2012) or high-to-mid latitude eddy-mean interactions (He et al. 2020), it needs further studies to determine the causality. It is noteworthy that the present study suggests the internal variability as a possible mechanism rather than the climate model-dependent bias and responses.

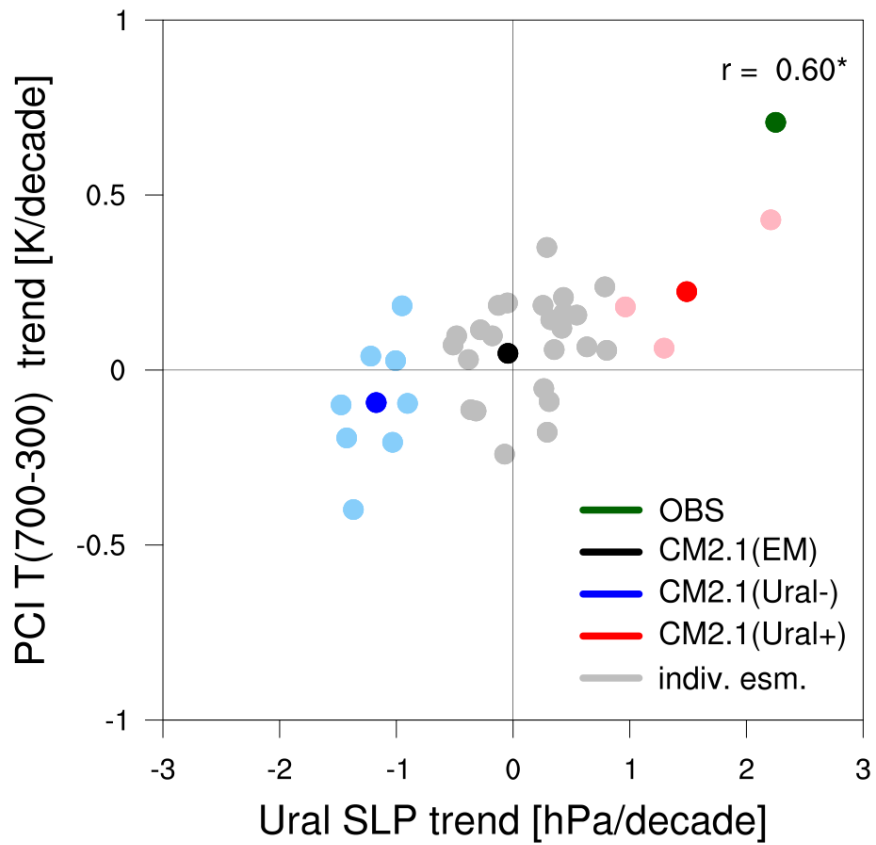


Figure 2.15. Same as Figure 2.11. but for the PCI_T averaged from 700 to 300 hPa.

2.5.4. Interannual variability in polar restoring experiments

One of the key points of the interannual-to-decadal WACE relationship is time lag between the Arctic and Eurasia. As state above, the BKS SIC anomalies in OND season is more related to the DJF Eurasian SAT anomalies compare to relationship with the concurrent SIC anomalies. This lead-lag relationship is one of the reasons why many of previous studies used Arctic sea ice forcing in climate simulations. Thus, the lead-lag relationship between the BKS SIC and Eurasia is re-examined in the polar restoring experiments (Fig. 2.16). While the observation shows clear time lag which peaks on OND season (green line in Fig. 2.16), there is no time lag between the BKS SIC and Eurasian SAT anomalies (black line). We further examine the Arctic-Eurasia relationship in Ural+ and Ural- ensemble groups. In both groups, there is no time lag between the BKS SIC and Eurasian SAT anomalies, while the Ural + ensembles have relatively larger correlation than in the Ural – ensembles. This is somewhat obvious since there is no clear relationship between the Arctic surface warming which is likely due to the Arctic sea ice loss and Ural SLP (Fig. 2.12). Additionally, the time-lagged relationship between the Arctic and Eurasia is often considered as an evidence of stratospheric pathway (Cohen et al. 2014; Kim et al. 2014). Since the GFDL CM2.1 model is low top model, the lagged relationship via stratosphere is missed in the model.

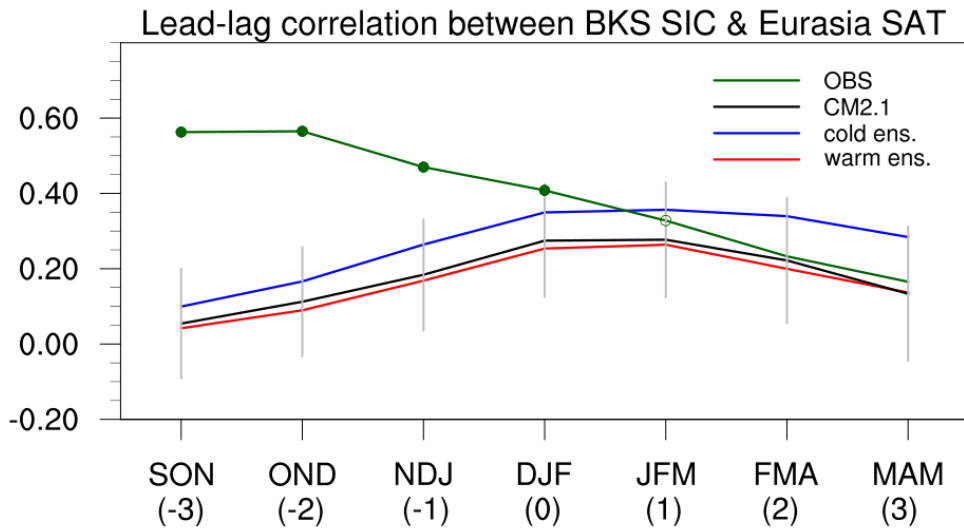


Figure 2.16. Lead-lag correlation between the BKS SIC and Eurasian SAT for the period of 1986-2015 in observation (green), the ensemble mean (black), Ural+ mean (blue), and Ural- mean (red). The ensemble spreads are denoted in grey bars.

The deeply extended Arctic warming is critical on both interannual and multi-decadal time scales (Fig. 2.14; Labe et al. 2020; He et al. 2020). This raise a question whether there is a governing mechanism covering for both interannual and multi-decadal WACE relationship or not. Thus we further show the relationship between the interannual relationship and long-term trend in Fig. 2.17. The color bars denote the same ensembles as in Fig. 2.11 and Fig. 2.12. The polar restoring experiments well capture the interannual relationship between the deep Arctic warming and the Ural SLP (compare black and green bars). Rather, the correlations in Ural + and Ural- group are both larger than the observed correlation between the vertically well-developed Arctic warming and Ural SLP. This is consistent with the previous studies showed that there is clear interannual co-variability between the tropospheric warming and Eurasian cold winter (Labe et al. 2020; He et al. 2020). However, in individual ensemble members (light color bars), there is no linear relationship between the interannual and long term trend in ensemble members. This result implies that the mechanisms regulate the interannual WACE relationship and their long term trend might differ, though they seem to occur by the similar dynamics.

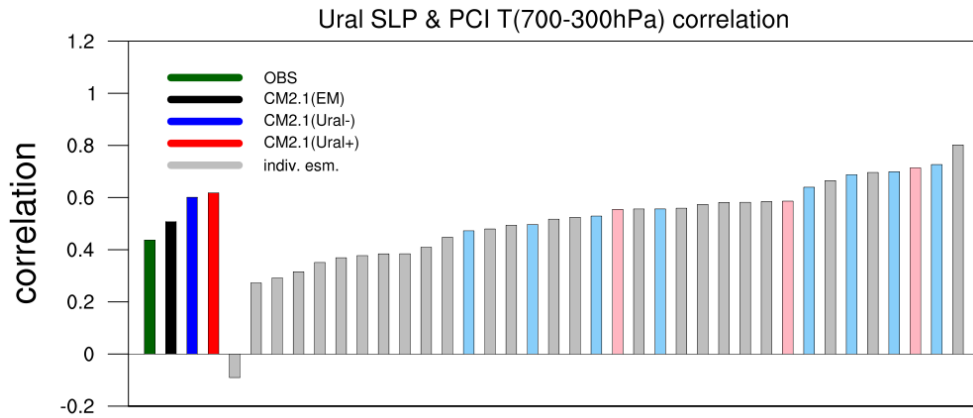


Figure 2.17. Correlation coefficient between the Ural SLP anomaly and PCI T anomaly averaged over the 700hPa to 300hPa for the period of 1986-2015 in observation (green), the ensemble mean (black), Ural+ mean (blue), Ural- mean (red), and individual ensembles (light colors). The Ural+ and Ural- ensemble members are denoted in light pink and light blue.

3. Summary and discussion

The Arctic-Eurasian SAT relationship has been examined from subseasonal to interannual-to-decadal time scale. On subseasonal time scale, a negative relationship between the BKS and Eurasian SAT anomalies is identified on a daily time scale. This relationship is primarily caused by synoptic weather systems over the Ural region. This is consistent with the previous studies that highlighted the role of the Ural blocking (Luo et al. 2016b; Yao et al. 2017; Tyrlis et al. 2020), but is more generalized as not only quasi-stationary blocking highs but also transient weather systems are considered in this study. It is further found that the dipolar SAT relationship is driven not only by the WACE cases but also by the CAWE cases. Both of them are frequently observed from November through February with a local minimum in late December, although what makes a local minimum is not clear.

It is found that the key process by which the Ural SLP anomaly determines temporal evolution of the WACE and CAWE cases is the horizontal temperature advection. Although previous studies often addressed the importance of the downward longwave radiation and surface heat flux especially on warm Arctic, the net radiative heating over the BKS, estimated from ERA-Interim model output, is negative. Its impact is mostly confined in the lower level. Note that the previous studies have considered only one or two terms in temperature budget (e. g., horizontal advection, surface fluxes, or downward long wave radiation; Panagiotopoulos et al. 2005; Mori et al. 2014; Ye and Messori 2020). In this study, all terms including horizontal advection,

adiabatic heating, and diabatic heating, are computed and the cancellation between the horizontal temperature advection and the diabatic heating is highlighted.

On interannual-to-decadal time scale, we investigate the interannual co-variability in Arctic and Eurasia. First we analyzed the relationship with Arctic sea ice and Eurasian SAT. The Eurasian winter SAT anomalies have maximum co-variability with the autumn BKS SIC anomalies with a time lag of approximately two months. Also, the Eurasian winter SAT have correlated with BKS SAT with a month lag. The 38 year is not enough long to understand the interannual variability and the independence of the BKS SIC related phenomena and the BKS SAT related phenomena. While the BKS SIC and BKS SAT have been tightly related, more samples are required to distinguish the mechanisms.

A coupled model is integrated by relaxing Arctic SST poleward of 70°N. This polar restoring experiment successfully reproduces Arctic warming from 1985 to 2016, but essentially no surface air temperature trend in midlatitude. This result indicates that Eurasian winter cooling in the recent decades is not likely a forced response to Arctic warming. No Eurasian temperature trend results from the cancellation between ensemble members with Eurasian cooling and those with warming. The former, characterized as warm Arctic-cold Eurasia (WACE) trend, typically accompanies the vertically well-organized Arctic warming, while the latter has shallow Arctic warming confined near the surface. This finding is consistent with idealized model, atmospheric general circulation model, and coupled model experiments on interannual WACE

relationship (Sellevold et al. 2016; He et al. 2020; Labe et al. 2020).

It is argued that the vertically well-extended Arctic warming effectively weakens the background wind. The weakened wind then allows more frequent and persistent Ural blockings (Yao et al. 2017; Luo et al. 2019). The resulting anticyclonic circulation drives Eurasia cooling while enhancing Arctic warming, through meridional temperature advection (Kim et al. 2021).

It is not clear what determines the vertical extent of Arctic warming. Since all ensemble members are forced by identical Arctic SST, it is likely set by atmospheric internal variability. Here it should be stated that the observed Arctic warming has a much deeper vertical extent than any ensemble members in this study. Since all forcings, except Arctic SST, are fixed constant in this study, deeper warming in the observation could result from greenhouse warming, aerosol forcing, and atmosphere-ocean circulations which have changed over time. The factor(s) that determines the vertical extent of Arctic warming in both the observation and climate models deserves further investigation.

The present study utilized only one model, i.e., GFDL-CM2.1. To test the robustness of the result, it would be useful to conduct similar experiments with multiple models. The high-top models, which fully resolve stratospheric processes, would be particularly useful. It has been argued that stratospheric processes are crucial for WACE-like temperature patterns (Kim et al. 2014; Nakamura et al. 2016; Zhang et al. 2018). The relative importance of stratospheric warming and tropospheric warming could be evaluated by comparing the simulations with high-top and low-top models.

References

- Barnes, E. A., Dunn-Sigouin, E., Masato, G., and Woollings, T. 2014 Exploring recent trends in Northern Hemisphere blocking. *Geophys. Res. Lett.*, 41(2), 638-644.
- Barnes E. A. and Screen J. A. 2015. The impact of Arctic warming on the midlatitude jet-stream: Can it? Has it? Will it? *Wiley Interdisciplinary Reviews: Climate Change* 6(3), 277-286, <https://doi.org/10.1002/wcc.337>.
- Barnes, E. A. and Polvani 2015 L. M. CMIP5 projections of Arctic amplification, of the North American/North Atlantic circulation, and of their relationship. *J. Clim.*, 28, 5254–5271.
- Blunden J. and Arndt D. S. (eds.) 2016. State of the Climate in 2015. *Bulletin of the American Meteorological Society*, 97(8), <https://doi.org/10.1175/2016BAMSStateoftheClimate.1>
- Blunden J. and Arndt D. S. (eds.) 2017. State of the Climate in 2016. *Bulletin of the American Meteorological Society*, 98(8), <https://doi.org/10.1175/2017BAMSStateoftheClimate.1>.
- Bond N. A., Overland J. E., Spillane M., and Stabeno P. 2003. Recent shift in the state of the North Pacific. *Geophysical Research Letters* 30(23), 2183, <https://doi.org/10.1029/2003GL018597>.
- Bretherton C. S., Smith C. and Wallace J. M. 1992. An intercomparison of methods for finding coupled patterns in climate data. *Journal of climate* 5(6), 541-560, [https://doi.org/10.1175/1520-0442\(1992\)005<0541:AIOMFF>2.0.CO;2](https://doi.org/10.1175/1520-0442(1992)005<0541:AIOMFF>2.0.CO;2).

- Bretherton, C. S., Widmann, M., Dymnikov, V. P., Wallace, J. M. and Bladé, I. 1999. The effective number of spatial degrees of freedom of a time-varying field, *Journal of climate* 12(7), 1990-2009.
- Cai, S., Hsu, P. C., and Liu, F. 2021 Changes in Polar Amplification in Response to Increasing Warming in CMIP6. *Atmospheric and Oceanic Science Letters*, 100043.
- Cavalieri D., Parkinson C., Gloersen P. and Zwally H. J. 1996. Sea ice concentrations from Nimbus-7 SMMR and DMSP SSM/I passive microwave data, <http://nsidc.org/data/nsidc-0051.html>. National Snow and Ice Data Center, Boulder, Colorado USA, <https://doi.org/10.5067/8GQ8LZQVL0VL>.
- Chang S. Y. and Perron P. 2016. A comparison of alternative methods to construct confidence intervals for the estimate of a break date in linear regression models. *Econometric Reviews*, 1-25, <https://doi.org/10.1080/07474938.2015.1122142>.
- Chen, X., Luo, D., Feldstein, S. B. and Lee, S. 2018. Impact of winter Ural blocking on Arctic sea ice: short-time variability. *Journal of climate* 31(6), 2267-2282.
- Chen H. W., Alley R. B. and Zhang F 2016. Interannual Arctic sea ice variability and associated winter weather patterns: A regional perspective for 1979–2014, *Journal of Geophysical Research–Atmospheres* 121(24), 14433-14455, <https://doi.org/10.1002/2016JD024769>.
- Cohen J. L., Furtado J. C., Barlow M. A., Alexeev V. A. and Cherry J. E. 2012a. Arctic warming, increasing snow cover and widespread boreal winter cooling. *Environmental Research Letters* 7(1), 014007, <https://doi.org/10.1088/1748-9326/7/1/014007>.

- Cohen J. L., Furtado J. C., Barlow M., Alexeev V. A. and Cherry J. E. 2012b. Asymmetric seasonal temperature trends. *Geophysical Research Letters* 39(4), <https://doi.org/10.1029/2011GL050582>.
- Cohen J. L., Screen J. A., Furtado J. C., Barlow M., Whittleston D., Coumou D., Francis J., Dethloff K., Entekhabi D., Overland J. and Jones J. 2014. Recent Arctic amplification and extreme mid-latitude weather. *Nature Geoscience* 7(9), 627-637, <https://doi.org/10.1038/ngeo2234>.
- Czaja A., and Frankignoul C. 2002. Observed impact of Atlantic SST anomalies on the North Atlantic Oscillation. *Journal of Climate* 15(6), 606-623. [https://doi.org/10.1175/1520-0442\(2002\)015<0606:OIOASA>2.0.CO;2](https://doi.org/10.1175/1520-0442(2002)015<0606:OIOASA>2.0.CO;2).
- Dee, D., et al. 2011. The ERA-Interim reanalysis: Configuration and performance of the data assimilation system, *Quarterly Journal of the Royal Meteorological Society* 137, 553–597, doi:10.1002/qj.828
- Delworth, T. L., Broccoli, A. J., Rosati, A., Stouffer, R. J., Balaji, V., Beesley, J. A., et al. 2006 GFDL's CM2 global coupled climate models. Part I: Formulation and simulation characteristics. *J. Clim.*, 19(5), 643-674.
- Deser, C., Tomas, R. A. and Sun, L. 2015; The role of ocean–atmosphere coupling in the zonal-mean atmospheric response to Arctic sea ice loss. *Journal of Climate* 28, 2168–2186.
- Dunn-Sigouin, E., Son, S. W., and Lin, H. 2013 Evaluation of Northern Hemisphere blocking climatology in the global environment multiscale model. *Mon. Weather Rev.*, 141(2), 707-727.
- Estrada F., Perron P. and Martínez-López B. 2013. Statistically derived contributions of diverse human influences to twentieth-century

temperature changes. *Nature Geoscience* 6(12), 1050-1055,
<https://doi.org/10.1038/ngeo1999>.

Francis J. A. and Vavrus S. J. 2012. Evidence linking Arctic amplification to extreme weather in mid-latitudes. *Geophysical Research Letters* 39(6),
<https://doi.org/10.1029/2012GL051000>.

Francis, J. A., and Vavrus, S. J. 2015 Evidence for a wavier jet stream in response to rapid Arctic warming. *Environ. Res. Lett.*, **10**(1), 014005.

Fuller W. A. 1976. *Introduction to Statistical Time Series*. New York: John Wiley and Sons.

Furtado, J. C., Cohen, J. L. and Tziperman, E. 2016 The combined influences of autumnal snow and sea ice on Northern Hemisphere winters. *Geophysical Research Letters* 43(7), 3478-3485.

García-Serrano J., Frankignoul C., Gastineau G. and Cámara A. 2015. On the Predictability of the Winter Euro-Atlantic Climate: Lagged Influence of Autumn Arctic Sea Ice. *Journal of Climate* 28(13), 5195–5216,
<https://doi.org/10.1175/JCLI-D-14-00472.1>.

Gong, T. and Luo, D. 2017. Ural blocking as an amplifier of the Arctic sea ice decline in winter. *Journal of Climate* 30(7), 2639-2654.

Hansen J., Ruedy R., Sato M. and Lo K. 2010. Global surface temperature change. *Reviews of Geophysics* 48(4),
<https://doi.org/10.1029/2010RG000345>.

He, S., Xu, X., Furevik, T., and Gao, Y. 2020 Eurasian cooling linked to the vertical distribution of Arctic warming. *Geophys. Res. Lett.*, **47**(10), e2020GL087212.

- Hersbach, H., Bell, B., Berrisford, P., Hirahara, S., Horányi, A., Muñoz-Sabater, J., et al. 2020. The ERA5 global reanalysis. *Q. J. Meteorol. Soc.*, **146**(730), 1999-2049.
- Honda M., Inoue J. and Yamane S. 2009. Influence of low Arctic sea-ice minima on anomalously cold Eurasian winters. *Geophysical Research Letters* **36**(8), L08707, <https://doi.org/10.1029/2008GL037079>.
- Hwang, J., Martineau, P., Son, S. W., Miyasaka, T., and Nakamura, H. 2020 The role of transient Eddies in North Pacific blocking formation and its seasonality. *J. Atmos. Sci.*, **77**(7), 2453-2470.
- Inoue J., Hori M. E. and Takaya K. 2012. The role of Barents Sea ice in the wintertime cyclone track and emergence of a warm-Arctic cold-Siberian anomaly. *Journal of Climate* **25**(7), 2561-2568, <https://doi.org/10.1175/JCLI-D-11-00449.1>.
- Jaiser R., Dethloff K. and Handorf D. 2013. Stratospheric response to Arctic sea ice retreat and associated planetary wave propagation changes. *Tellus Series A* **65**(1), 19375, <https://doi.org/10.3402/tellusa.v65i0.19375>.
- Jung, T., Kasper, M. A., Semmler, T. and Serrar, S. 2014. Arctic influence on subseasonal midlatitude prediction. *Geophysical Research Letters* **41**(10), 3676-3680.
- Kaufmann R. K., Kauppi H., Mann M. L. and Stock J. H. 2011. Reconciling anthropogenic climate change with observed temperature 1998–2008. *Proceedings of the National Academy of Sciences* **108**(29), 11790-11793, <https://doi.org/10.1073/pnas.1102467108>.
- Kim D. and Perron P. 2009. Assessing the relative power of structural break tests using a framework based on the approximate Bahadur slope.

Journal of Econometrics 149, 26-51,
<https://doi.org/10.1016/j.jeconom.2008.10.010>.

- Kim K. Y. and Son S. W. 2016. Physical characteristics of Eurasian winter temperature variability. *Environmental Research Letters* 11, 044009, <https://doi.org/10.1088/1748-9326/11/4/044009>.
- Kim B. M., Son S. W., Min S. K., Jeong J. H., Kim S. J., Zhang X., Shim T. and Yoon J. H. 2014. Weakening of the stratospheric polar vortex by Arctic sea-ice loss. *Nature communications* 5, 4646, <https://doi.org/10.1038/ncomms5646>.
- King M. P., Hell M. and Keenlyside N. 2016. Investigation of the atmospheric mechanisms related to the autumn sea ice and winter circulation link in the Northern Hemisphere. *Climate dynamics* 46(3-4), 1185-1195, <https://doi.org/10.1007/s00382-015-2639-5>.
- Kim, K. Y., Kim, J. Y., Kim, J., Yeo, S., Na, H., Hamlington, B. D. and Leben, R. R. 2019. Vertical feedback mechanism of winter Arctic amplification and sea ice loss. *Scientific Reports* 9(1), 1-10.
- Kim, H., Yeh, S. W., An, S. I., Park, J. H., Kim, B. M., and Baek, E. H. 2020 Arctic Sea ice loss as a potential trigger for Central Pacific El Niño events. *Geophys. Res. Lett.*, **47**(7), e2020GL087028.
- Kosaka Y. and Xie S. P. 2013. Recent global-warming hiatus tied to equatorial Pacific surface cooling. *Nature* 501(7467), 403, <https://doi.org/10.1038/nature12534>.
- Kug J. S., Jeong J. H., Jang Y. S., Kim B. M., Folland C. K., Min S. K. and Son S. W. 2015. Two distinct influences of Arctic warming on cold winters over North America and East Asia. *Nature Geoscience* 8(10), 759, <https://doi.org/10.1038/NCEO2517>.

- Labe, Z., Peings, Y., and Magnusdottir, G. 2020 Warm Arctic, cold Siberia pattern: Role of full Arctic amplification versus sea ice loss alone. *Geophys. Res. Lett.*, **47**(17), e2020GL088583.
- Li C., Stevens B. and Marotzke J. 2015. Eurasian winter cooling in the warming hiatus of 1998–2012. *Geophysical Research Letters* **42**(19), 8131-8139, <https://doi.org/10.1002/2015GL065327>.
- Liu J., Curry J. A., Wang H., Song M. and Horton R. M. 2012. Impact of declining Arctic sea ice on winter snowfall. *Proceedings of the National Academy of Sciences* **109**(11), 4074-4079, <https://doi.org/10.1073/pnas.1114910109>.
- Luo, D., Xiao, Y., Yao, Y., Dai, A., Simmonds, I. and Franzke, C. L. 2016. Impact of Ural blocking on winter warm Arctic–cold Eurasian anomalies. Part I: Blocking-induced amplification, *Journal of Climate* **29**(11), 3925-3947.
- Luo, D., Xiao, Y., Diao, Y., Dai, A., Franzke, C. L. and Simmonds, I. 2016. Impact of Ural blocking on winter warm Arctic–cold Eurasian anomalies. Part II: The link to the North Atlantic Oscillation. *Journal of Climate* **29**(11), 3949-3971.
- Luo, D., Yao, Y., Dai, A., Simmonds, I. and Zhong, L. 2017. Increased quasi stationarity and persistence of winter Ural blocking and Eurasian extreme cold events in response to Arctic warming. Part II: A theoretical explanation. *Journal of Climate* **30**(10), 3569-3587.
- Luo, D., Chen, X., Dai, A. and Simmonds, I. 2018. Changes in atmospheric blocking circulations linked with winter Arctic warming: A new perspective, *Journal of Climate* **31**(18), 7661-7678.
- Luo, B., Wu, L., Luo, D., Dai, A. and Simmonds, I. 2019. The winter midlatitude-Arctic interaction: effects of North Atlantic SST and high-latitude

blocking on Arctic sea ice and Eurasian cooling. *Climate Dynamics* 52(5-6), 2981-3004.

Matsumura, S. and Kosaka Y. 2019. Arctic-Eurasian climate linkage induced by tropical ocean variability. *Nature Communications* 10, 3441, <https://doi.org/10.1038/s41467-019-11359-7>.

McCusker K. E., Fyfe J. C. and Sigmond M. 2016. Twenty-five winters of unexpected Eurasian cooling unlikely due to Arctic sea-ice loss. *Nature Geoscience* 9(11), 838-842, <https://doi.org/10.1038/ngeo2820>.

Meehl G. A., Arblaster J. M., Fasullo J. T., Hu A. and Trenberth K. E. 2011. Model-based evidence of deep-ocean heat uptake during surface-temperature hiatus periods. *Nature Climate Change* 1(7), 360, <https://doi.org/10.1038/NCLIMATE1229>.

Meehl G. A., Hu A., Arblaster J. M., Fasullo J. and Trenberth K. E. 2013. Externally forced and internally generated decadal climate variability associated with the Interdecadal Pacific Oscillation. *Journal of Climate* 26(18), 7298-7310, <https://doi.org/10.1175/JCLI-D-12-00548.1>.

Meehl G. A., Teng H. and Arblaster J. M. 2014. Climate model simulations of the observed early-2000s hiatus of global warming. *Nature Climate Change* 4(10), 898, <https://doi.org/10.1038/nclimate2357>.

Mori M., Kosaka Y., Watanabe M., Nakamura H. and Kimoto M. 2019. A reconciled estimate of the influence of Arctic sea-ice loss on recent Eurasian cooling. *Nature Climate Change*, 9, 123-129, <https://doi.org/10.1038/s41558-018-0379-3>.

Mori M., Watanabe M., Shiogama H., Inoue J. and Kimoto M. 2014. Robust Arctic sea-ice influence on the frequent Eurasian cold winters in past decades, *Nature Geoscience* 7(12), 869-873, <https://doi.org/10.1038/ngeo2277>.

- Nakamura T., Yamazaki K., Iwamoto K., Honda M., Miyoshi Y., Ogawa Y., Tomikawa Y., Ukita J. 2016. The stratospheric pathway for Arctic impacts on midlatitude climate. *Geophysical Research Letters* 43(7), 3494-3501, <https://doi.org/10.1002/2016GL068330>.
- Ogawa F., Keenlyside N., Gao Y., Koenigk T., Yang S., Suo L., ... and Omrani N. E. 2018. Evaluating impacts of recent Arctic sea ice loss on the Northern Hemisphere winter climate change. *Geophysical Research Letters* 45, 3255-3263, <https://doi.org/10.1002/2017GL076502>.
- Outten S. D. and Esau I. 2012. A link between Arctic sea ice and recent cooling trends over Eurasia. *Climatic Change* 110(3-4), 1069-1075, <https://doi.org/10.1007/s10584-011-0334-z>.
- Overland J., Francis J. A., Hall R., Hanna E., Kim S. J. and Vihma T. 2015. The melting Arctic and midlatitude weather patterns: Are they connected? *Journal of Climate* 28(20), 7917-7932, <https://doi.org/10.1175/JCLI-D-14-00822.1>.
- Overland, J. E., and Wang, M. 2015 Increased variability in the early winter subarctic North American atmospheric circulation. *J. Clim.*, **28**(18), 7297-7305.
- Panagiotopoulos, F., Shahgedanova, M., Hannachi, A., and Stephenson, D. B. 2005. Observed trends and teleconnections of the Siberian high: A recently declining center of action. *Journal of Climate* 18(9), 1411-1422.
- Park, D. S. R., Lee, S. and Feldstein, S. B. 2015. Attribution of the recent winter sea ice decline over the Atlantic sector of the Arctic Ocean. *Journal of Climate* 28(10): 4027-4033.
- Peings Y. and Magnusdottir G. 2014. Response of the wintertime Northern Hemisphere atmospheric circulation to current and projected Arctic

sea ice decline: A numerical study with CAM5. *Journal of Climate* 27(1), 244-264, <https://doi.org/10.1175/JCLI-D-13-00272.1>.

Perron P. and Yabu T. 2009. Testing for shifts in trend with an integrated or stationary noise component. *Journal of Business & Economic Statistics* 27, 369-396, <https://doi.org/10.1198/jbes.2009.07268>.

Petoukhov V. and Semenov V. A. 2010. A link between reduced Barents-Kara sea ice and cold winter extremes over northern continents. *Journal of Geophysical Research-Atmospheres* 115(D21), <https://doi.org/10.1029/2009JD013568>.

Sato, K., Inoue, J., and Watanabe, M. 2014. Influence of the Gulf Stream on the Barents Sea ice retreat and Eurasian coldness during early winter. *Environmental Research Letters* 9(8), 084009.

Screen, J. A., Deser, C., and Simmonds, I. 2012 Local and remote controls on observed Arctic warming. *Geophys. Res. Lett.*, **39**(10).

Screen, J. A. and Francis, J. A. 2016. Contribution of sea-ice loss to Arctic amplification is regulated by Pacific Ocean decadal variability. *Nature Climate Change* 6, 865-861.

Screen J. A. 2017. Simulated Atmospheric Response to Regional and Pan-Arctic Sea Ice Loss. *Journal of Climate* 30(11), 3945-3962, <https://doi.org/10.1175/JCLI-D-16-0197.1>.

Screen J. A., Deser C., Smith D. M., Zhang X., Blackport R., Kushner P. J., ... and Sun L. 2018. Consistency and discrepancy in the atmospheric response to Arctic sea-ice loss across climate models. *Nature Geoscience* 11(3), 155, <https://doi.org/10.1038/s41561-018-0059-y>.

- Sellekvold, R., Sobolowski, S., and Li, C. 2016 Investigating possible Arctic–midlatitude teleconnections in a linear framework. *J. Clim.*, **29**(20), 7329-7343.
- Sorokina, S. A., Li, C., Wettstein, J. J. and Kvamstø, N. G. 2016. Observed atmospheric coupling between Barents Sea ice and the warm-Arctic cold-Siberian anomaly pattern. *Journal of Climate* **29**(2), 495-511.
- Sun L., Perlwitz J. and Hoerling M. 2016. What caused the recent “Warm Arctic, Cold Continents” trend pattern in winter temperatures?, *Geophysical Research Letters*, **43**(10), 5345–5352, <https://doi.org/10.1002/2016GL069024>.
- Sung, M. K., Kim, S. H., Kim, B. M., and Choi, Y. S. 2018. Interdecadal variability of the warm Arctic and cold Eurasia pattern and its North Atlantic origin. *Journal of Climate* **31** (15), 5793-5810.
- Tang Q., Zhang X., Yang X. and Francis J. A. 2013. Cold winter extremes in northern continents linked to Arctic sea ice loss. *Environmental Research Letters* **8**(1), 014036, <https://doi.org/10.1088/1748-9326/8/1/014036>.
- Thompson D.W., Wallace J.M. and Hegerl G.C. 2000. Annular Modes in the Extratropical Circulation. Part II: Trends. *Journal of Climate* **13**(5), 1018–1036, [https://doi.org/10.1175/1520-0442\(2000\)013<1018:AMITEC>2.0.CO;2](https://doi.org/10.1175/1520-0442(2000)013<1018:AMITEC>2.0.CO;2).
- Tibaldi, S., and Molteni, F. 1990. On the operational predictability of blocking. *Tellus A*, **42**(3), 343-365.
- Tyrlis, E., Bader, J., Manzini, E., Ukita, J., Nakamura, H. and Matei, D. 2020. On the role of Ural Blocking in driving the Warm Arctic–Cold Siberia pattern *Quarterly Journal of the Royal Meteorological Society*.

- Wallace J. M., Smith C. and Bretherton C. S. 1992. Singular value decomposition of wintertime sea surface temperature and 500-mb height anomalies. *Journal of climate*, 5(6), 561-576, [https://doi.org/10.1175/1520-0442\(1992\)005<0561:SVDOWS>2.0.CO;2](https://doi.org/10.1175/1520-0442(1992)005<0561:SVDOWS>2.0.CO;2).
- Walsh J. E. 2014. Intensified warming of the Arctic: Causes and impacts on middle latitudes. *Global and Planetary Change* 117, 52-63, <https://doi.org/10.1016/j.gloplacha.2014.03.003>.
- Wang, J., Kim, H. M. and Chang, E. K. 2017. Changes in Northern Hemisphere winter storm tracks under the background of Arctic amplification. *Journal of Climate* 30(10), 3705-3724.
- Woollings, T., Barriopedro, D., Methven, J., Son, S. W., Martius, O., Harvey, B., et al. 2018 Blocking and its response to climate change. *Current Climate Change Reports*, 4(3), 287-300.
- Wu, B., Handorf, D., Dethloff, K., Rinke, A. and Hu, A. 2013. Winter weather patterns over northern Eurasia and Arctic sea ice loss. *Monthly Weather Review* 141(11), 3786-3800.
- Wu Y. and Smith K. L. 2016. Response of Northern Hemisphere midlatitude circulation to Arctic amplification in a simple atmospheric general circulation model. *Journal of Climate* 29(6), 2041-2058, <https://doi.org/10.1175/JCLI-D-15-0602.1>.
- Xu X., Li F., He S. and Wang H. 2018. Subseasonal Reversal of East Asian Surface Temperature Variability in Winter 2014/15. *Advanced in Atmospheric Sciences*, 35(6), 737-752, <https://doi.org/10.1007/s00376-017-7059-5>.

- Xu, X., He, S., Gao, Y., Furevik, T., Wang, H., Li, F., and Ogawa, F. 2019
Strengthened linkage between midlatitudes and Arctic in boreal
winter. *Clim. Dyn.*, **53**(7), 3971-3983.
- Yang, W., and Magnusdottir, G. 2018 Year-to-year variability in Arctic
minimum sea ice extent and its preconditions in observations and the
CESM large ensemble simulations. *Sci. Rep.*, **8**(1), 1-7.
- Yao, Y., Luo, D., Dai, A. and Simmonds, I. 2017. Increased quasi stationarity and
persistence of winter Ural blocking and Eurasian extreme cold events
in response to Arctic warming. Part I: Insights from observational
analyses., *Journal of Climate* **30**(10), 3549-3568.
- Ye, K. and Messori, G. 2020. Two leading modes of wintertime atmospheric
circulation drive the recent warm Arctic–cold Eurasia temperature
pattern., *Journal of Climate* **33**(13), 5565-5587.
- Yu, L., Zhong, S., Sui, C., and Sun, B. 2020. Revisiting the trend in the
occurrences of the “warm Arctic–cold Eurasian continent”
temperature pattern. *Atmospheric Chemistry and Physics* **20**(22),
13753-13770.
- Zhang X., Sorteberg A., Zhang J., Gerdes R. and Comiso J. C. 2008. Recent radical
shifts of atmospheric circulations and rapid changes in Arctic climate
system. *Geophysical Research Letters*, **35**(22),
<https://doi.org/10.1029/2008GL035607>.
- Zhang, X., Lu, C., and Guan, Z. 2012. Weakened cyclones, intensified
anticyclones and recent extreme cold winter weather events in
Eurasia. *Environmental Research Letters* **7**(4), 044044.

Zhang P., Wu Y. and Smith K. L. 2018. Prolonged effect of the stratospheric pathway in linking Barents–Kara Sea sea ice variability to the midlatitude circulation in a simplified model. *Climate Dynamics* 50(1-2), 527-539, <https://doi.org/10.1007/s00382-017-3624-y>.

Zhang, P., Wu, Y., Simpson, I. R., Smith, K. L., Zhang, X., De, B., and Callaghan, P. 2018 A stratospheric pathway linking a colder Siberia to Barents-Kara Sea sea ice loss. *Sci. Adv.*, **4**(7), eaat6025.

국문초록

북극과 유라시아 기후 변동성 사이의 계절내, 경년 및 장기트렌드 관계

김 혜 진
지구환경과학부
박사과정
서울대학교

북극과 유라시아 지표 기온은 계절내 규모에서 장기 트렌드에 이르기까지 다양한 시간 규모에서 높은 통계적 연관성을 보인다. 본 연구에서는 크게 계절내 규모와 경년 및 장기 변동성으로 구분하여 이러한 연관성을 설명하는 메커니즘을 재검증하였다. 먼저 북극과 유라시아 기온 사이의 계절내 변동성의 경우, 11월부터 2월까지의 추운 계절에만 발생하며 12월에 약화되는 계절 변동성이 나타나는 것을 확인하였다. 기존 연구에서는 계절내 규모의 북극-유라시아 기온 변동성을 좌우하는 것은 우랄 지역의 블로킹에 의해 유도된 따뜻한 북극-차가운 유라시아 기온 패턴이라고 알려져 왔으나, 반대 사례인 차가운 북극-따뜻한 유라시아 기온 패턴 역시 겨울철에 나타남을 확인하였다. 즉 본 연구 결과는 북극과 유라시아 기온의 계절내 변동성을 좌우하는 것은 우랄 블로킹이 아닌, 우랄 지역을 지나가는 기상 시스템을 확인하였다. 또한 경년 및 장기 트렌드 시간 규모에서 역시 북극과 유라시아 기온 사이의 높은 연관성이 나타난다. 가을철부터 급격하게 감소하는 북극 해빙이 최근 겨울철의 급격한 기온 감소현상의 원인으로 지목되었으며, 통계분석 결과 경년 및 장기 트렌드 시간 규모에서 높은 연관성을 보임을 정량적으로 검증하였다. 그러나 모형 실험 결과 북극 해빙은 겨울철 유라시아의 기온 변동성을 야기하는 원인으로는 충분하지 않음을 확인하였다. 오히려 북극 해빙을 실험에 반영하였을 때, 북극 기온의 변화가 연직으

로 잘 발달하는 일부 실험에서만 유라시아에 강한 기온 감소 현상이 나타나는 것이 확인되었다. 이 결과는 유라시아 겨울철 기온 감소현상이 대기 내부 변동성에 크게 의존하고 있음을 시사한다.

주요어: 따뜻한 북극-차가운 유라시아 패턴, 우랄 블로킹, 북극 해빙 감소, 대기 내부 변동성

학 번: 2016-37590